iScience

CellPress
OPEN ACCESS

Article

Ubiquitin-specific protease 7 inhibitors reveal a differentiated mechanism of p53-driven anti-cancer activity

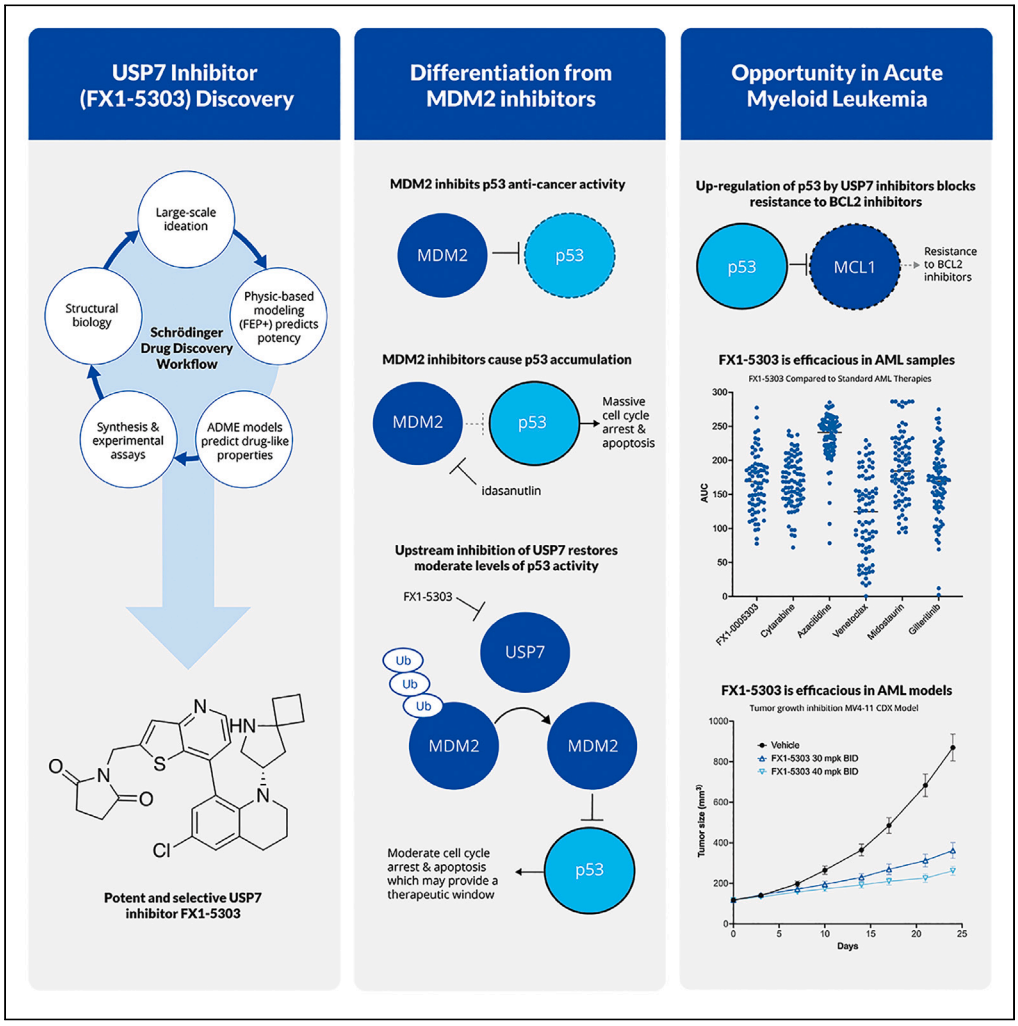

Alan S. Futran, Tao Lu, Katherine Amberg-Johnson, ..., Karen Akinsanya, David Madge, Kristian K. Jensen

futran@gmail.com (A.S.F.)
tlu101@yahoo.com (T.L.)

Highlights

New USP7 inhibitors discovered using Schrödinger's enumeration workflow and FEP+

USP7 inhibitors elucidate the effects of different patterns of p53 induction

USP7 inhibitors demonstrate activity in models of AML, including patient samples

USP7 inhibitors have potential for clinical use and utility as chemical probes

Futran et al., iScience 27, 109693
May 17, 2024
https://doi.org/10.1016/j.isci.2024.109693

iScience

CellPress
OPEN ACCESS

Article

Ubiquitin-specific protease 7 inhibitors reveal a differentiated mechanism of p53-driven anti-cancer activity

Alan S. Futran,[1,6,7,*] Tao Lu,[2,6,*] Katherine Amberg-Johnson,[1] Jiayi Xu,[1] Xiaoxiao Yang,[2] Saidi He,[2] Sarah Boyce,[1] Jeffrey A. Bell,[1] Robert Pelletier,[1] Takao Suzuki,[2] Xianhai Huang,[1] Heng Qian,[2] Liping Fang,[2] Li Xing,[2] Zhaowu Xu,[2] Stephen E. Kurtz,[3,4] Jeffrey W. Tyner,[3,5] Wayne Tang,[1] Tao Guo,[2] Karen Akinsanya,[1] David Madge,[2] and Kristian K. Jensen[1]

SUMMARY

The USP7 deubiquitinase regulates proteins involved in the cell cycle, DNA repair, and epigenetics and has been implicated in cancer progression. USP7 inhibition has been pursued for the development of anti-cancer therapies. Here, we describe the discovery of potent and specific USP7 inhibitors exemplified by FX1-5303. FX1-5303 was used as a chemical probe to study the USP7-mediated regulation of p53 signaling in cells. It demonstrates mechanistic differences compared to MDM2 antagonists, a related class of anti-tumor agents that act along the same pathway. FX1-5303 synergizes with the clinically approved BCL2 inhibitor venetoclax in acute myeloid leukemia (AML) cell lines and *ex vivo* patient samples and leads to strong tumor growth inhibition in *in vivo* mouse xenograft models of multiple myeloma and AML. This work introduces new USP7 inhibitors, differentiates their mechanism of action from MDM2 inhibition, and identifies specific opportunities for their use in the treatment of AML.

INTRODUCTION

Ubiquitin-specific protease 7 (USP7) is a deubiquitinating enzyme (DUB) that cleaves ubiquitin from a range of substrates, shielding them from degradation by the proteasome and otherwise regulating their function. USP7 substrates play important roles in several cellular processes including cell cycle regulation, maintaining genomic stability, and epigenetic control.[1] USP7 activity has been implicated in cancer progression and the immune response[2] and its overexpression is associated with tumor aggressiveness and poor prognosis in a variety of cancer types.[3–5] Genetic and pharmacological inhibition of USP7 have been shown to inhibit the growth of a number of different tumor cell lines,[6–9] making USP7 inhibition an attractive strategy for the treatment of cancer.

USP7 acts on a wide range of substrates, but its role in regulating the MDM2/p53 axis has drawn the most interest due to its ability to promote the degradation of the critical p53 tumor suppressor (Figure 3A). MDM2 is an E3 ubiquitin ligase that ubiquitinates p53, marking it for degradation by the proteasome. USP7 deubiquitinates and stabilizes MDM2, which promotes p53 degradation.[10] In addition to its role in regulating p53, USP7 activity has been implicated in several other pathways related to tumor progression. This includes roles regulating FOXP3,[11] which promotes T-regulatory cell development and function, and other key tumor drivers and suppressors, including DNMT1,[12] N-Myc,[13] and EZH2/PRC2.[14] USP7 has over 20 reported substrates,[15] and several cancer cell lines carrying p53-inactivating mutations are sensitive to USP7 inhibitors, indicating that mechanisms unrelated to p53 activity may contribute to their anti-tumor activity.[14,16] However, studies using a potent, specific, covalent inhibitor of USP7 have shown that, when tested across a broad panel of cancer cells lines, cellular responses were predicted by *TP53* mutation status and that *TP53* knockout rescues the inhibitor-induced suppression of cell growth.[15] This indicates that the anti-tumor activity of USP7 inhibition is primarily driven by the stabilization of p53.

Therapeutic strategies that induce p53 activity have been the subject of intense research for decades.[17] MDM2 antagonists work along the same pathway as USP7 inhibitors by blocking the MDM2/p53 interaction, thereby preventing p53 ubiquitination and degradation and leading to p53 accumulation in cells. Several MDM2 inhibitors are under evaluation in clinical trials and have demonstrated clinical activity; however,

[1]Schrödinger, 1540 Broadway 24th Floor, New York, NY, USA
[2]WuXi AppTec, 288 Fute Zhong Road, Waigaoqiao Free Trade Zone, Shanghai 200131, China
[3]Knight Cancer Institute, Oregon Health & Science University, Portland, OR, USA
[4]Division of Hematology & Medical Oncology, Department of Medicine, Oregon Health & Science University, Portland, OR, USA
[5]Department of Cell, Developmental & Cancer Biology, Oregon Health & Science University, Portland, OR, USA
[6]These authors contributed equally
[7]Lead contact
*Correspondence: futran@gmail.com (A.S.F.), tlu101@yahoo.com (T.L.)
https://doi.org/10.1016/j.isci.2024.109693

agents in this class have faced challenges with respect to tolerability, and no MDM2 inhibitor has been approved for clinical use.[18,19] Thus, alternative therapeutic strategies that can induce p53 activity while avoiding the safety liabilities of MDM2 antagonists would be attractive.

Several groups have identified potent, selective inhibitors of USP7.[7–9,14,15,20] None have entered clinical trials, and developing improved compounds for clinical development and identifying suitable indications for their use remain important goals. Here, we report the structure-guided development of selective inhibitors of USP7 with potent anticancer activity, exemplified by FX1-5303. Using FX1-5303, we illustrate mechanistic differences between USP7 and MDM2 inhibitors and their effects on p53 signaling. While both mechanisms act along the USP7/MDM2/p53 axis, the magnitude and duration of their effects on p53 activity in cells differ. We explore how differences between MDM2 and USP7 inhibitors could impact their relative potencies in healthy and neoplastic cells and use them as chemical tools to illuminate fundamental aspects of p53 regulation and activity in cells. We show that FX1-5303 is efficacious in acute myeloid leukemia (AML) cell lines and *ex vivo* AML patient samples. It also demonstrates synergistic activity with the clinically approved BCL2 inhibitor venetoclax in AML cell lines and patient samples, and we show that this synergy can be explained by inhibitor-induced reductions in MCL1. Finally, we demonstrate *in vivo* tumor growth inhibition following the oral administration of FX1-5303 in mouse xenograft models. Overall, these data highlight the therapeutic potential of USP7 inhibitors, show their utility as chemical probes to study p53 biology, and reveal specific opportunities for their use in the treatment of AML.

RESULTS

Structure-based drug discovery of tetrahydroquinoline bi-aryl series of ubiquitin-specific protease 7 inhibitors

We identified a series of tetrahydroquinoline bi-aryl USP7 inhibitors, exemplified by compound FX1-3763, using Schrödinger's enumeration workflow and free energy perturbation calculation (FEP+)[21–23] (Figure S1A). The tetrahydroquinoline (C-ring) was hand-drawn and subsequently profiled using FEP+ potency prediction, which suggested this modification would be tolerated. Optimization of the basic amine position was carried out using our proprietary *de novo* design workflow, AutoDesigner,[23] where we screened upwards of a billion compounds *in silico*, leading to the discovery of the potent spiro-pyrrolidine. The overall hit rate for compounds coming out of the *de novo* design workflow that met both our criteria for novelty, potency, and physicochemical properties was quite low, making it even more remarkable that the compound discovered by this approach had all the attributes required to become our lead compound. A co-crystal structure of the catalytic domain of USP7 with FX1-3763 at 2.26 Å resolution was obtained. FX1-3763 binds to USP7 similarly to other reported allosteric inhibitors[7–9,14,15] at the intersection of the palm and thumb subdomains, stabilizing the inactive form of USP7 with a disrupted catalytic site (residues C223, H464, D481) and the regulatory switching loop (residues 283–295) positioned to block ubiquitin binding (Figure 1A). Key interactions with the side chain of residues D295 and N297, the backbone N-H of V296 and F409, and the backbone carbonyl of M292 were observed and conserved for all potent compounds in this chemical series (Figure 1B). Our FEP+ modeling-guided medicinal chemistry efforts enabled the development of optimized tetrahydroquinoline bi-aryl USP7 inhibitors, exemplified by FX1-5303 (Figure 2A).

FX1-5303 inhibits USP7 with an IC_{50} = 0.29 nM in a USP7 biochemical activity assay (Figure 2B), and its potency was confirmed in an orthogonal surface plasmon resonance (SPR) binding assay (Figure S2A). Its cellular potency was determined by measuring the p53 accumulation (EC_{50} = 5.6 nM) and inhibition of cell viability (IC_{50} = 15 nM) in the MM.1S multiple myeloma (MM) cell line, which was previously shown to be sensitive to USP7 inhibitors[24] (Figures 2C and 2D). Across all of the USP7 inhibitors tested, biochemical potency was well-correlated with p53 induction and cell viability inhibition (Figure S2B), indicating that compounds' cellular activity is on-target and driven by USP7 inhibition. These compounds are highly selective; in a panel of 44 DUBs, only USP7 was inhibited by FX1-5303, and similar results were obtained for three other related compounds (Figures 2E and S2C). These potent, selective compounds were used to probe the USP7 inhibition mechanism of action.

Ubiquitin-specific protease 7 inhibitors induce a modest and transient increase of p53 in cells

USP7 knockdown and pharmacological inhibition have been shown to upregulate p53 (Figure 3A), and cancer cell line panel viability screens have demonstrated that *TP53* mutational status is a key predictor of sensitivity to USP7 inhibition.[14–16] To better understand the mechanism of action of USP7 inhibitors and to identify differences with MDM2 antagonists, we studied the dynamic effects of both agents on downstream target engagement markers.

As expected, FX1-5303 treatment led to a dose-dependent decrease in MDM2 levels, followed by an increase in p53 and the p53 target gene, p21, in multiple cell lines (Figures 3B and S3A–S3C). p53 accumulation in MM.1S cells was transient, with levels peaking 2–6 h after treatment with FX1-5303 and nearly returning to basal levels after 24 h. This transient increase was also reflected in the levels of the p53 target, p21 (Figure 3B). This effect was not specific to MM.1S cells, as we observed a similar transient pattern of p53 and p21 induction in response to FX1-5303 in MV4-11 cells (Figure S3A).

We compared the kinetics and magnitude of p53 accumulation induced by FX1-5303 and idasanutlin, a MDM2 inhibitor currently in clinical trials. The maximum increases of p53 and p21 detected in MM.1S cells after FX1-5303 treatment were approximately 3-fold and 6-fold above DMSO-treated cells, respectively. In contrast, idasanutlin-treated MM.1S cells showed maximum increases of approximately 20-fold in p53 and 80-fold in p21 compared to DMSO-treated cells. In contrast to FX1-5303, idasanutlin leads to sustained increases in p53 and p21. After 24h of idasanutlin treatment, p53 remains elevated approximately 14-fold, while in FX1-5303-treated cells p53 returns nearly to basal levels at this time point (Figure 3B). While both idasanutlin and FX1-5303 act along the USP7/MDM2/p53 pathway to block p53 degradation, direct MDM2 inhibition with idasanutlin led to much larger and more sustained increases in p53 activity compared to the upstream inhibition of USP7 with FX1-5303.

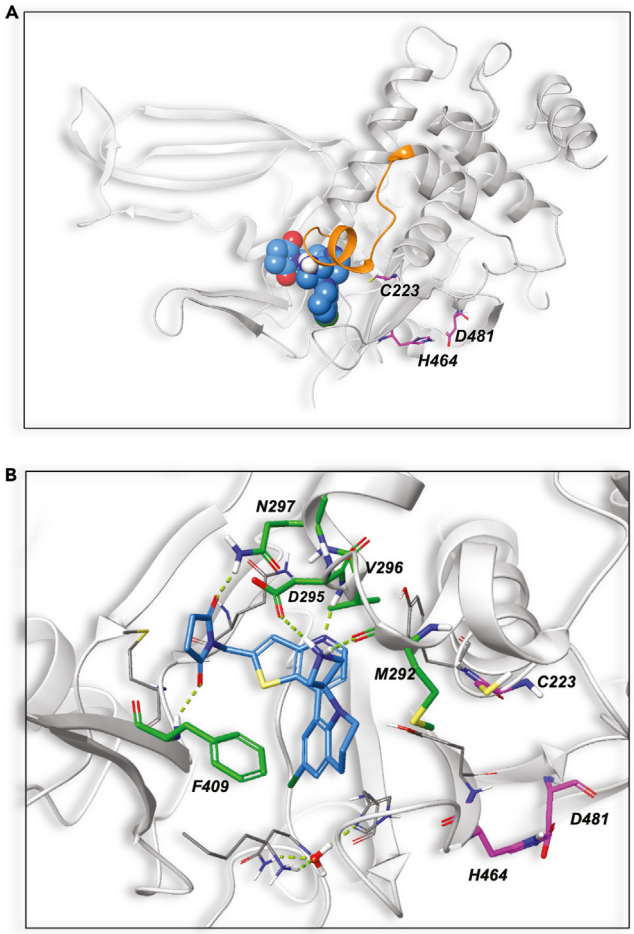

Figure 1. Structural Basis of USP7 Inhibitor Binding

(A) Crystal structure of the catalytic domain of USP7 in the inactive, inhibitor-bound conformation shown with disrupted catalytic site residues (*pink*) and allosteric inhibitor FX1-3763 (*space-filling*), PDB code 8D4Z.

(B) Binding site detail of the USP7 inhibitor FX1-3763 (*blue*) shown with key interactions to the following residues (*green*): M292 backbone carbonyl, V296 backbone nitrogen, N297 side chain; F409 edge-to-face pi-stacking with ligand bi-aryl core; D295 salt bridge to azetidine basic amine. Catalytic residues (*pink*) adjacent to the allosteric binding site shown for clarity.

This effect cannot be easily attributed to a difference in potency of these compounds, since both idasanutlin and FX1-5303 inhibit the cell viability of MM1.S cells equipotently (Figure S4B). Instead, these findings highlight significant mechanistic differences between the effects of our USP7 inhibitors and MDM2 inhibitors in cells. Thus, these agents can be leveraged as chemical probes to understand the downstream effects of different perturbations on p53 signaling.

Transient p53 induction by USP7 inhibitors selectively targets TP53 WT cancer cells over healthy cells

We explored whether the distinct p53 induction profiles induced by USP7 and MDM2 inhibitors lead to differential downstream effects in cells. In addition to illuminating fundamental properties of p53 regulation and activity, any differences could have implications for the application of these different p53-inducing therapeutic strategies. A liability for the clinical application of p53 activating therapies is the risk of toxicities brought on by the induction of p53 in healthy cells, including diarrhea, nausea, and myelosuppression, which have been observed in phase 1 clinical trials with idasanutlin.[25,26] Since FX1-5303 induces lower levels of p53 than idasanutlin, we hypothesized that this could translate into differential effects in healthy and malignant cells.

To test this hypothesis, we first confirmed that healthy cells also induce less p53 and p21 when treated with FX1-5303 compared to idasanutlin using healthy human PBMCs (Figure 4A). Since PBMCs do not readily proliferate, we next compared the anti-proliferative effects of FX1-5303 and idasanutlin in the MRC5 cell line, a model of healthy human fibroblasts. Live cell imaging of MRC5 cells over 5 days in the presence of FX1-5303 or idasanutlin showed significant differences (Figure 4B). Cell confluency increased monotonically when grown in the presence of 1 μM FX1-5303, though at a decreased rate relative to DMSO-treated cells. In contrast, when the MRC5 cells were treated with 1 μM

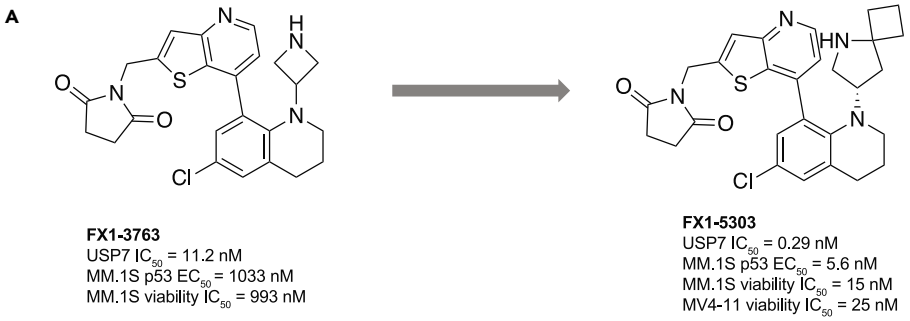
A
FX1-3763
USP7 IC50 = 11.2 nM
MM.1S p53 EC50 = 1033 nM
MM.1S viability IC50 = 993 nM
FX1-5303
USP7 IC50 = 0.29 nM
MM.1S p53 EC50 = 5.6 nM
MM.1S viability IC50 = 15 nM
MV4-11 viability IC50 = 25 nM

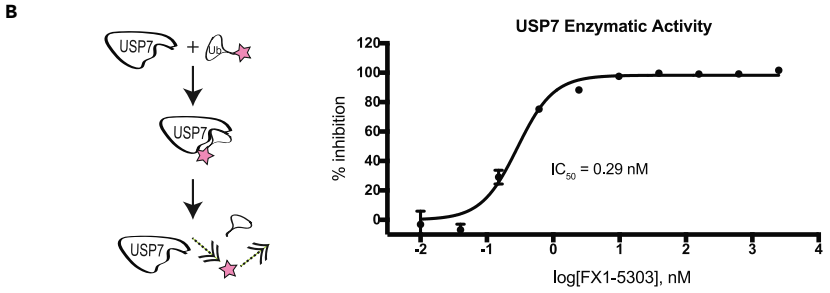
B
USP7
Ub
USP7 Enzymatic Activity
% inhibition
IC50 = 0.29 nM
log[FX1-5303], nM

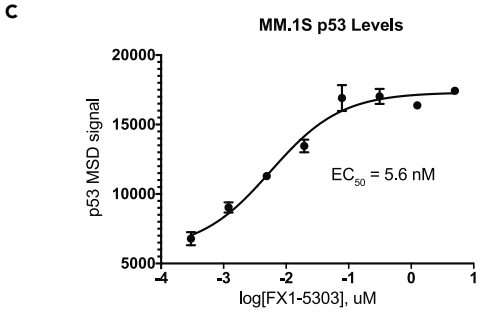
C
MM.1S p53 Levels
p53 MSD signal
EC50 = 5.6 nM
log[FX1-5303], uM

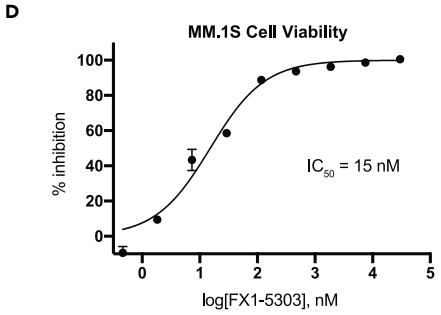
D
MM.1S Cell Viability
% inhibition
IC50 = 15 nM
log[FX1-5303], nM

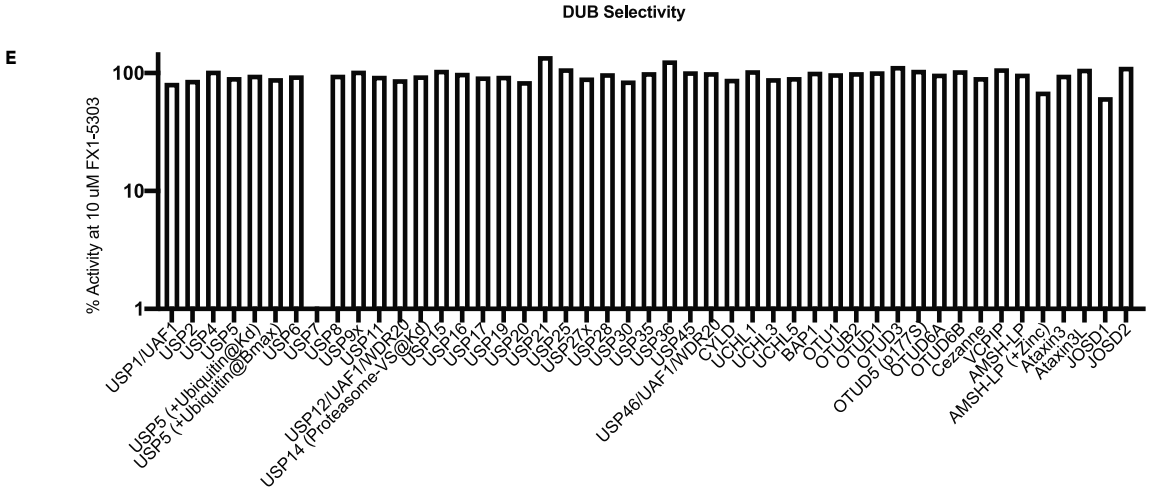
E
DUB Selectivity
% Activity at 10 uM FX1-5303
USP1/UAF1
USP2
USP4
USP5
USP5 (+Ubiquitin@K0)
USP5 (+Ubiquitin@Bmax)
USP6
USP7
USP8
USP9x
USP11
USP12/UAF1/WDR20
USP14 (Proteasome-VS@K0)
USP15
USP16
USP17
USP19
USP20
USP21
USP25
USP27x
USP28
USP30
USP35
USP36
USP45
USP46/UAF1/WDR20
CYLD
UCHL1
UCHL3
UCHL5
BAP1
OTUB1
OTUB2
OTUD1
OTUD3
OTUD5 (p17/S)
OTUD6A
OTUD6B
Cezanne
VCPIP
AMSH-LP
AMSH-LP (+Zinc)
Ataxin3
Ataxin3L
JOSD1
JOSD2

Figure 2. *in vitro* activity and selectivity of USP7 Inhibitors

(A) Optimization of FX1-3763 led to the identification of FX1-5303.

(B) (Left) Schematic of USP7 biochemical assay. Cleavage of the ubiquitin substrate by USP7 deubiquitinase activity leads to fluorescence. (Right) Activity of FX1-5303 in USP7 biochemical assay.

(C) MM1.S cells were treated with FX1-5303 for 4 h after which p53 levels were quantified.

(D) MM1.S cells were treated with FX1-5303 for three days, after which viability was measured using Cell Titer Glo (CTG).

(E) Activity of 44 deubiquitinase targets after treatment with 10 μM FX1-5303 (DUBprofiler, Ubiquigent).

In all graphs, error bars represent the standard deviation from the mean.

idasanutlin, confluency remained static, increasing by less than 10% over the 5-day time course. This was associated with lower p53 levels induced by FX1-5303 compared to idasanutlin (Figure 4D). In contrast, both FX1-5303 and idasanutlin fully inhibited growth of the MM.1S cancer cell line at 1 μM (Figure 4C). Idasanutlin and FX1-5303 exhibit similar potencies inhibiting cell viability in MM.1S cells (Figure S4B); therefore, the differential effects observed in fibroblast cell lines when both agents were tested at 1 μM reflect fundamental differences in their mechanisms, as opposed to differences in concentration relative to their IC_{50}.

While MRC5 cells are a convenient model of healthy cells, isogenic cell lines with differential p53 activity provide an opportunity to directly compare how p53 levels control anti-proliferative sensitivity to USP7 and MDM2 inhibitors. The RKO colon cancer cell line is a *TP53* WT cell line that was potently inhibited by idasanutlin (IC_{50} = 170 nM). This is surprising, as RKO cells are insensitive to FX1-5303 (IC_{50} = 3.4 μM) and other USP7 inhibitors[14] despite clear target engagement as measured by p53 accumulation (Figure S4C). To confirm that the anti-proliferative effects of idasanutlin were related to the induction of p53 and not an alternative mechanism, we tested the MDM2 inhibitor in the isogenic RKO-E6 cell line. This cell line carries the HPV E6 oncogene, which reduces p53 activity.[27] The IC_{50} of idasanutlin in RKO-E6 cells was shifted over 50-fold relative to the parental cell line, while the IC_{50} of FX1-5303 was essentially unchanged (Figure 4E). This indicates that MDM2 inhibitor activity in the RKO cell line is on target and related to the induction of p53, and that the more modest induction of p53 elicited by USP7 inhibition is insufficient to inhibit proliferation in this cell line.

These findings highlight significant mechanistic differences between the effects of MDM2 inhibitors and USP7 inhibitors in healthy and neoplastic cells. While both compounds inhibit the growth of MM and AML cell lines with comparable potencies, some cell types – including fibroblasts, a model of normal, healthy human cells – are better able to proliferate in the presence of USP7 inhibitors.

Ubiquitin-specific protease 7 inhibitors demonstrate potent anti-proliferative activity in acute myeloid leukemia cells

Potent, selective USP7 inhibitors emerged from various groups in the past several years. Some of these agents have been screened in broad cancer cell line panels; however, more extensive characterization of these compounds in cellular models of *TP53* WT cancers has been limited to fewer indications, including MM and Ewing sarcoma.[14,15] To understand the potential clinical utility of USP7 inhibitors, we sought to test their activity in malignancies that are characterized by *TP53* WT mutational status and high unmet medical need. AML is an indication that fits these criteria. Studies have suggested that USP7 inhibition could be an effective strategy for the treatment of AML.[6] However, these studies employed the tool compound P22077[28] which is a non-selective (inhibits both USP7 and USP47) and relatively weak (>1μM IC_{50} in cellular viability assays of p53 WT cell lines[28] compared to <50 nM IC_{50} for FX1-5303) inhibitor of USP7. We sought to confirm the activity of USP7 inhibition in models of AML using our potent and selective inhibitors and further characterize the efficacy of the mechanism of action in this indication.

FX1-5303 demonstrated potent antiproliferative activity in *TP53* WT AML cell lines, including MV4-11 and OCI-AML-3, but lacked significant activity in the *TP53* mutant HL-60 cell line (Figure 5A). Encouraged by the activity in *TP53* WT AML cell lines, we further characterized the activity of FX1-5303 in a panel of 74 *ex vivo* samples from patients with hematological malignancies including myelodysplastic syndrome (MDS), chronic lymphocytic leukemia (CLL), acute lymphocytic leukemia (ALL), and AML (Figure S5). FX1-5303 inhibited the growth of patient samples with comparable potency to approved AML therapies (Figure 5C) and was most potent in samples derived from patients with AML (Figure 5B). Because only 2/74 patient samples contained a mutation in TP53 (with only one sample containing a confirmed loss-of-function mutation), we were unable to compare the relative activity of FX1-5303 in *TP53*-WT and *TP53*-null samples. Overall, the observed activity of FX1-5303 in AML cell lines and *ex vivo* patient samples shows promise for USP7 inhibition in this indication.

Ubiquitin-specific protease 7 inhibitors are synergistic with the BCL2 inhibitor venetoclax

We next sought to explore rational combinations of USP7 inhibitors with other agents used in the treatment of AML. BCL2 inhibitors synergize with MDM2 inhibitors in preclinical models of AML,[29,30] and this combination is under investigation in clinical trials.[26,31] The overexpression of MCL1 is a frequent mechanism of resistance to BCL2 inhibitors.[32] p53 activation by MDM2 inhibitors can promote the degradation of MCL1, which may explain their synergy in combination with BCL2 inhibitors.[30] We hypothesized that the USP7 inhibitor-induced accumulation of p53 could similarly potentiate the activity of BCL2 inhibitors.

We investigated the effect of combining FX1-5303 with the BCL2 inhibitor venetoclax in AML cell lines. The OCI-AML-3 cell line expresses high levels of MCL1 and is inherently resistant to venetoclax. In this cell line, the combination of FX1-5303 and venetoclax led to strong anti-proliferative effects, with a combination index (CI) and Bliss synergy score consistent with strong synergy (Figures 6A, 6B, and S6A). Synergy between FX1-5303 and venetoclax was also observed in MV4-11 cells and the combination index (CI average = 0.6) was similar to the published combination index for Idasanutlin and Venetoclax in MV4-11 cells (CI = 0.72) (Figure S6B). USP7 inhibitor-insensitive RKO cells demonstrated no synergy between FX1-5303 and venetoclax (Figure S6C). To confirm the mechanism of synergy, we measured the effect of FX1-5303

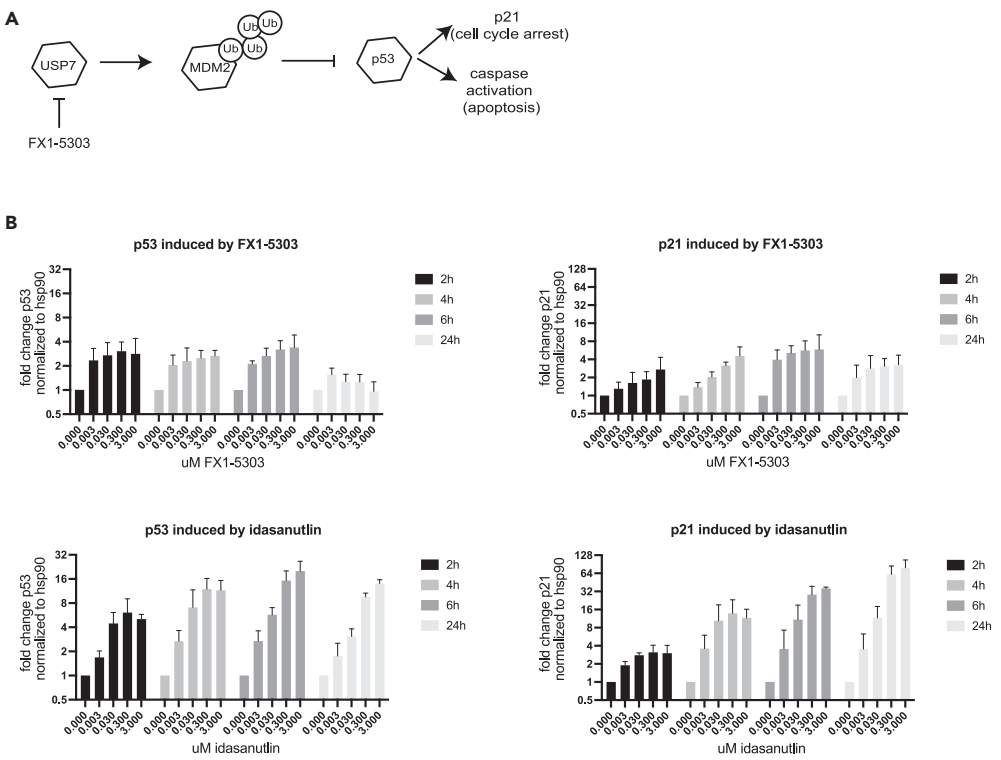

Figure 3. Effects of USP7 and MDM2 Inhibitors on p53 Induction

(A) Schematic showing the molecular mechanism of USP7 inhibitors. Inhibition of USP7 blocks its ability to deubiquitinate MDM2, inducing the degradation of MDM2. Since MDM2 is an E3 ubiquitin-ligase that marks p53 for degradation, loss of MDM2 blocks p53 degradation and leads to increased p53 activity.

(B) Time course of p53 (left) and p21 (right) levels after treatment with FX1-5303 (top) and idasanutlin (bottom) in MM1.S cells.

In all graphs, error bars represent the standard deviation from the mean.

and venetoclax on MCL1. Venetoclax induces an increase in MCL1 levels in OCI-AML3 cells, but this increase is reversed when venetoclax is co-dosed with FX1-5303 (Figure 6C). FX1-5303 also potentiates the activity of venetoclax in AML patient samples. As shown in Figure 6D, the median AUC of the combination of the two agents in the patient samples was significantly below that of each individual compound (p = 4.9E-07 by wilcoxon signed rank test, Figure S6D). This confirms that USP7 inhibition can strengthen the activity of venetoclax in a more translatable model of AML.

Ubiquitin-specific protease 7 inhibitors are efficacious *in vivo* in mouse cell-line-derived xenograft models of multiple myeloma and acute myeloid leukemia

MM.1S and MV4-11 cell-line-derived xenograft (CDX) mouse models were used to test the *in vivo* activity of orally dosed FX1-5303. FX1-5303 treatment was generally well-tolerated (Figure S7) and effectively inhibited MM.1S and MV4-11 tumor growth. Twice daily dosing of 30 mg/kg FX1-5303 for 24 days resulted in the 95% tumor growth inhibition of MM.1S tumors (Figure 7A). Twice daily dosing of 30 mg/kg and 40 mg/kg FX1-5303 for 24 days resulted in 68% and 72% tumor growth inhibition of MV4-11 tumors, respectively (Figure 7D). Treatment with FX1-5303 resulted in an increase in pharmacodynamic markers for USP7 inhibition and p53 induction. MIC-1, a secreted biomarker of p53 activity,[33] was measured in the urine of FX1-5303-treated mice over three time periods on day 24 of both studies, and elevated levels of the marker at all three time points indicate sustained p53 activity (Figures 7B and 7E). On the final day of dosing, mice were sacrificed 2 h post dosing (MM.1S) or 4 h post dosing (MV4-11), and tumors were collected to measure levels of p21 and p53. In both MM.1S and MV4-11 CDX tumors, p53 levels were elevated in mice treated with FX1-5303, though the effect was modest. However, p21 levels in these tumors were significantly higher than tumors from untreated mice (Figures 7C and 7F), indicating that targets of p53 were activated in tumors of mice treated with the USP7 inhibitor.

DISCUSSION

USP7 has drawn considerable interest as a target for novel cancer therapies. However, no USP7 inhibitors have entered clinical trials, and substantial questions remain regarding the mechanism of action and whether clinical indications can be identified that are well-suited for intervention with a USP7 inhibitor. Here, we report the identification of a potent series of tetrahydroquinoline bi-aryl USP7 inhibitors and

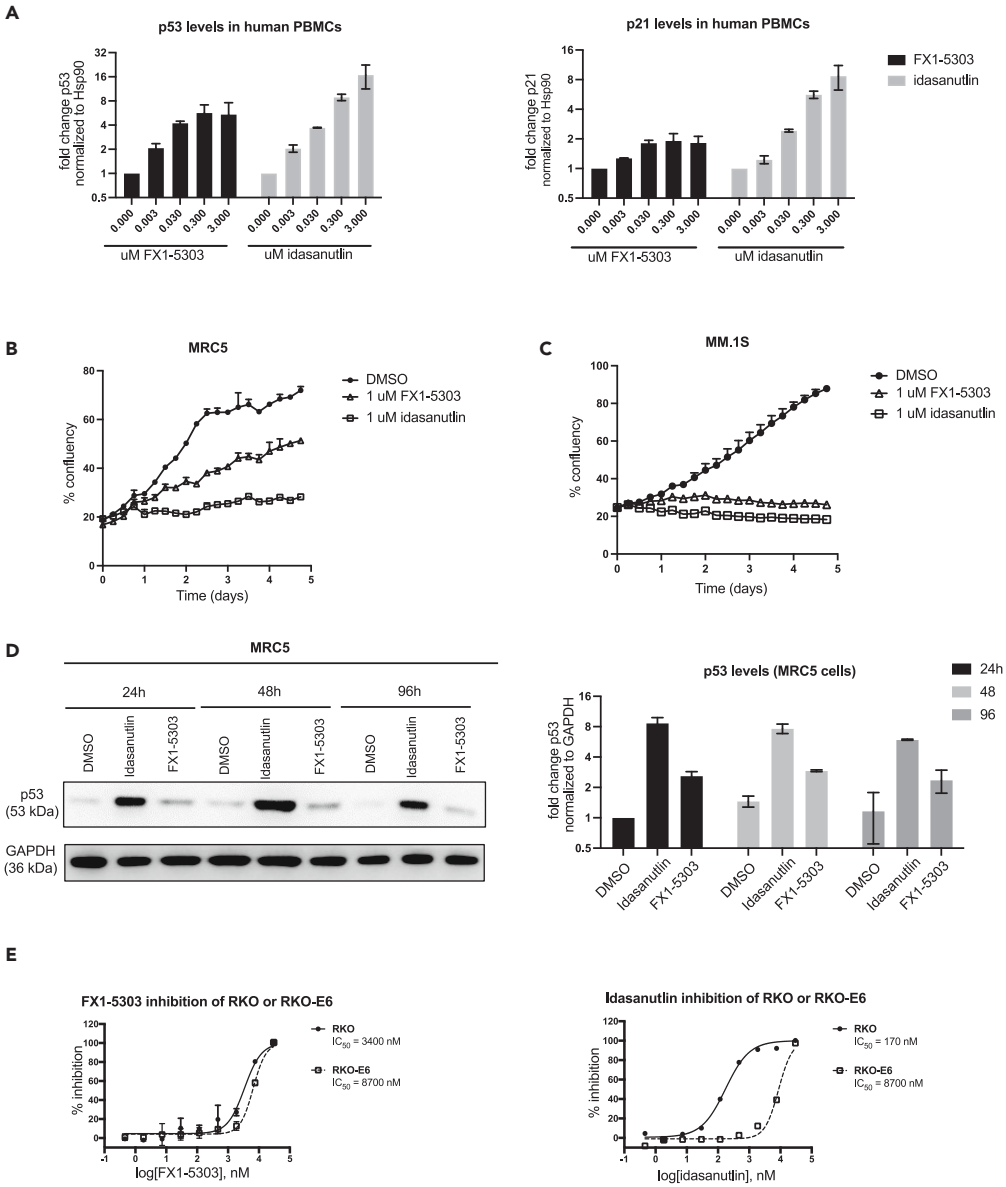

Figure 4. Differential Effects of USP7 and MDM2 Inhibitors in Healthy and Neoplastic Cells

(A) Human PBMCs were treated with FX1-5303 or idasanutlin for 4 h p53 and p21 were measured by Western blot.

(B) MRC5 or (C) MM.1S cells were treated with 1 μM FX1-5303, 1 μM idasanutlin or DMSO control. Growth was measured over 5-day using an incucyte to measure % confluency.

(D) MRC5 cells were treated with 1 μM FX1-5303 and 1 μM idasanutlin and p53 levels were measured by Western blot. A representative Western blot is shown on the left and quantification is shown on the right.

(E) RKO and RKO-E6 cells were treated with FX1-5303 or idasanutlin for three days, after which viability was measured using CTG.

In all graphs, error bars represent the standard deviation from the mean.

demonstrate their anti-cancer activity in models of AML, synergy with the BCL2 inhibitor venetoclax, and a differentiated mechanism of action that could provide benefits over MDM2 antagonists.

We used FX1-5303 to probe the effects of USP7 inhibitors in cells. Compared to idasanutlin, treatment with FX1-5303 led to a more modest and transient induction of p53. Increased p53 activity drives the expression of MDM2 and its own degradation as part of a negative feedback loop.[34] USP7 inhibition may preserve elements of this negative feedback loop while MDM2 inhibition does not. USP7 inhibitors do not directly block the function of MDM2, they instead prevent the deubiquitination of MDM2. Therefore, any MDM2 that is not marked with ubiquitin is not affected by USP7 inhibition. In contrast, MDM2 inhibitors, such as idasanutlin, directly block the function of MDM2 by occluding the p53-binding pocket. This does not preserve any of the p53 negative feedback loop, because it inactivates all MDM2 in the cell, including MDM2

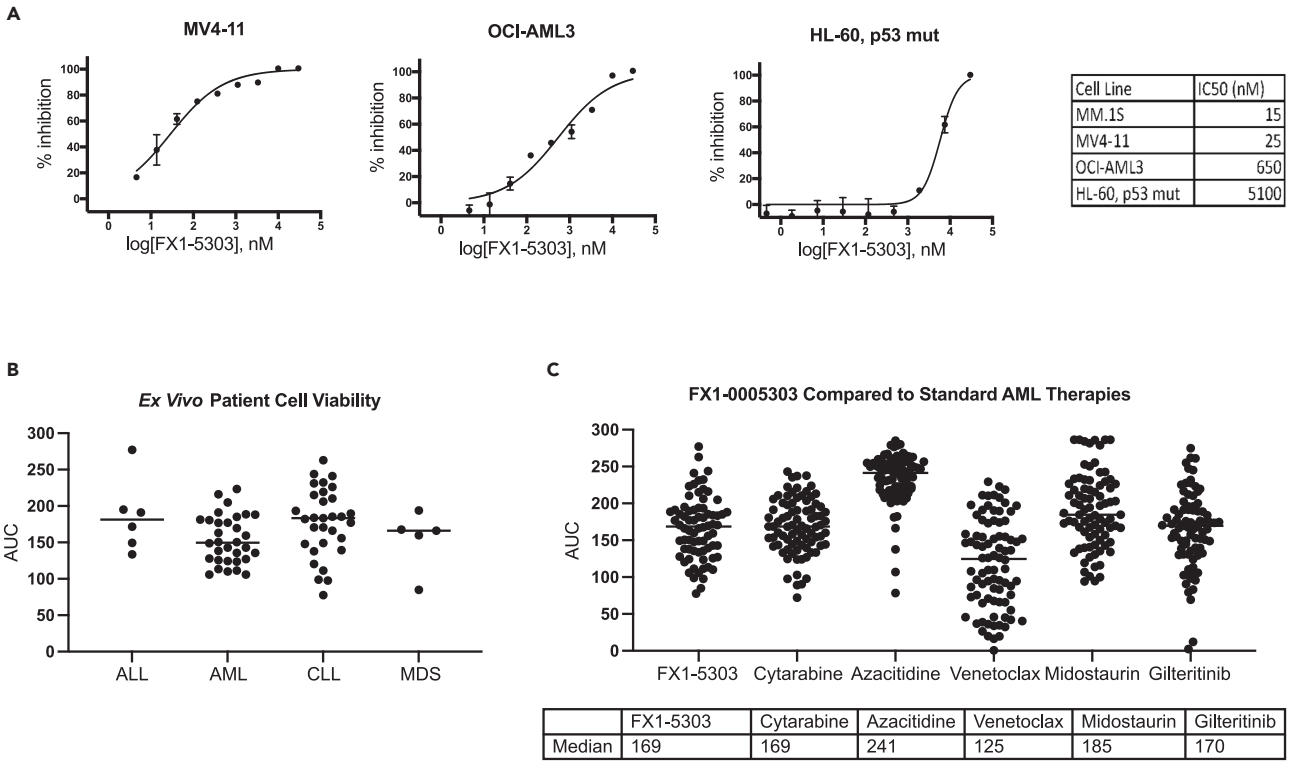

Figure 5. Activity of FX1-5303 in AML Cells

(A) AML cell lines MV4-11 (*TP53* WT), OCI-AML3 (*TP53* WT), and HL-60 (*TP53* mutated) were treated with FX1-5303 for five days, after which viability was measured using CTG. Error bars represent the standard deviation from the mean.

(B) Patient cells with the indicated hematological malignancies were treated with a range of concentrations of FX1-5303 *ex vivo* for 3 days after which viability was measured using an MTS assay. The potency of the inhibition of cell viability was quantified by the area under the curve (AUC) of the dose-response curve.

(C) Patient cells were treated *ex vivo* with a range of concentrations of FX1-5303, cytarabine, azacitidine, venetoclax, midostaurin, and gilteritinib. Viability was measured after 3 days using an MTS assay. Potency of FX1-5303 as measured by AUC is compared to these reference standard-of-care drugs.

newly expressed in response to increased p53 activity. We believe that the more modest and transient increase in p53 accumulation observed in response to FX1-5303 compared to idasanutlin may be due to the ability of USP7 inhibitors to preserve elements of the p53/MDM2 negative feedback loop.

p53 activity in the cell is dynamic, and, depending on the stimulus and the resulting pattern of p53 activation, this activity can lead to different cellular outcomes. For example, in response to γ-irradiation, p53 levels increase in pulses. These pulses are of the same duration and amplitude, but their frequency is proportional to the dose of γ-radiation.[35] In contrast, exposure to UV radiation leads to a single pulse of p53 activity with a dose-dependent amplitude and duration.[36] Pulsed p53 - such as that induced by γ-irradiation - has been shown to lead to transient cell-cycle arrest, while sustained p53 - such as that induced by UV-irradiation or treatment with MDM2 inhibitors - leads to terminal fates such as apoptosis or permanent cell-cycle arrest (senescence).[37] This highlights the importance of understanding the dynamics of p53 induction in response to pharmacological intervention and its differing effects on healthy and malignant cells. Selective USP7 inhibitors such as FX1-5303 provide a novel chemical tool to study changes in p53 regulation, including the effects of transient increases in p53 levels in the cell, and contrast the effects of USP7 inhibition with those of other genetic, pharmacological, or radiation-induced perturbations.

We explored whether differences in the way USP7 inhibition and MDM2 inhibition affect the MDM2/p53 axis translate to differences in anti-proliferative activity in healthy and malignant cells. While idasanutlin and FX1-5303 show very similar potency in inhibiting the viability of sensitive MM and AML cell lines, idasanutlin showed significantly greater anti-proliferative activity against RKO cells and healthy human fibroblast cell lines. Differential sensitivity to different degrees of p53 induction could provide a benefit in a clinical setting if healthy cells tolerate the more modest increase in p53 elicited by USP7 inhibitors relative to MDM2 antagonists. MDM2 inhibitors under clinical evaluation commonly cause gastrointestinal and hematologic adverse events that are likely related to p53 induction.[19] Inhibition of USP7 is an alternative therapeutic strategy for the induction of p53, and we hypothesize that the more limited induction of p53 elicited by USP7 inhibitors in cells compared to MDM2 inhibitors may spare healthy cells. Further studies are required to understand the relevance of these differences to safety and efficacy and whether this can result in a better therapeutic index. These findings also highlight the utility of leveraging novel pharmacological agents that act on the p53 pathway as chemical probes to understand the differential effects of distinct patterns of p53 regulation in different cellular contexts.

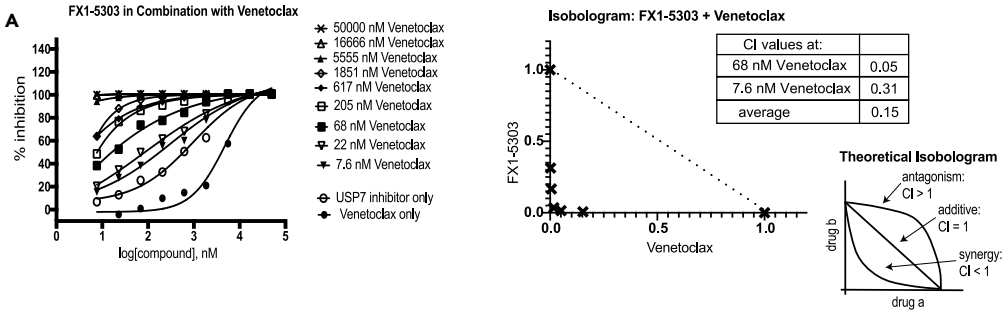

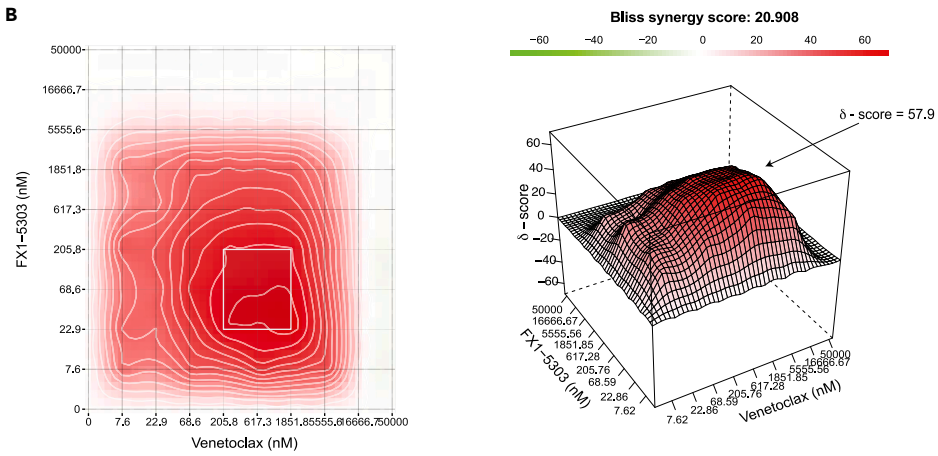

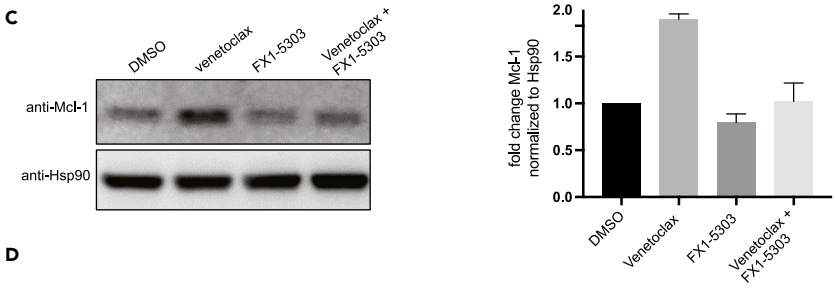

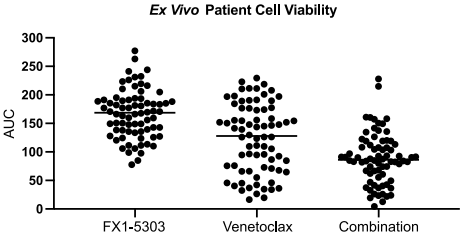

	FX1-5303	Venetoclax	Combination
Number of values	74	74	74
Minimum	77.6	16.5	4.48
25% Percentile	136	70.0	59.2
Median	169	128	86.2
75% Percentile	191	176	115
Maximum	277	229	228
Range	200	213	223
Mean	167	124	88.5
Std. Deviation	42.3	60.4	44.8
Std. Error of Mean	4.92	7.03	5.20

Figure 6. FX1-5303 Exhibits Synergy with Venetoclax

(A) (Left) OCI-AML3 cells were treated in dose-response with FX1-5303 at a range of doses of venetoclax for five days and cell viability was measured with CTG. (Right) Normalized isobolograms were generated and combination indices (CI) were calculated using the Loewe Additivity Model. (Inset) Theoretical isobologram that illustrates synergistic, additive, and antagonistic drug combinations.

(B) Bliss synergy scores were calculated using Synergy Finder. Matrix (left) and topology graph (right) indicate the level of synergy for each dose combination.

(C) OCI-AML3 cells were treated with 1 μM venetoclax, 1 μM FX1-5303, or 1 μM of venetoclax +1 μM FX1-5303. Western blot samples were taken at 4 h post treatment. Error bars represent the standard deviation from the mean.

(D) Patient cells were treated *ex vivo* with a range of concentrations of FX1-5303, venetoclax, or FX1-5303 and venetoclax in equidose combination. Viability was measured after 3 days using an MTS assay. Data are plotted on the left and summary statistics are charted on the right.

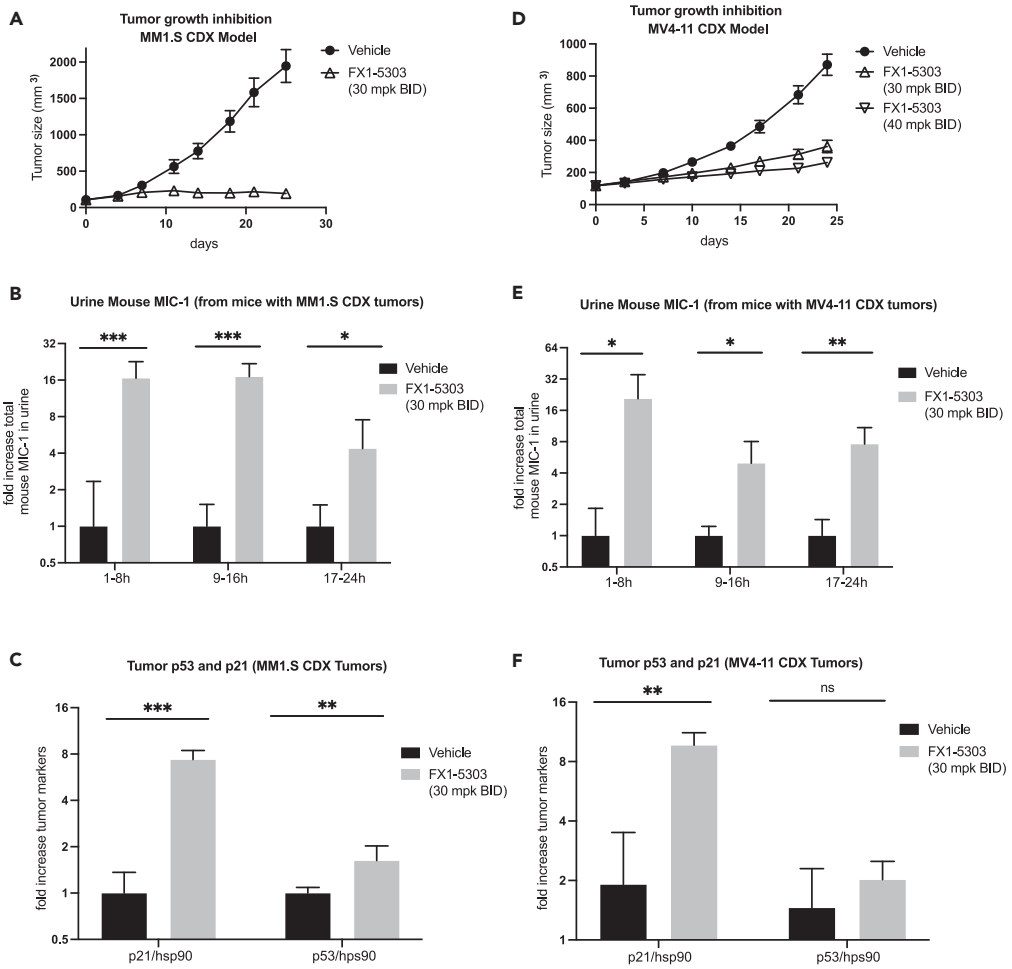

Figure 7. *in vivo* Activity of FX1-5303

(A) CB-17 SCID mice engrafted with MM.1S tumors were treated with the indicated dose of FX1-5303 or vehicle and tumor volume was monitored.

(B) On the final day of dosing, urine was collected at three different time intervals from FX1-5303- or vehicle-treated mice engrafted with MM1.S tumors. Mouse MIC-1 from urine was quantified by ELISA as a measure of target engagement.

(C) After the final dose, MM1.S tumors were dissected, and Western blot was used to measure levels of p53 and p21.

(D) CB-17 SCID mice engrafted with MV4-11 tumors were treated with the indicated doses of FX1-5303 or vehicle and tumor volume was monitored.

(E) On the final day of dosing, urine was collected at three different time intervals from FX1-5303- or vehicle-treated mice engrafted with MV4-11 tumors. Mouse MIC-1 from urine was quantified by ELISA as a measure of target engagement.

(F) After the final dose, MV4-11 tumors were dissected, and Western blot was used to measure levels of p53 and p21.

Significance was measured using a multiple unpaired t-test (GraphPad Prism), with $n = 8$ animals per group, where * = p-value <0.05, ** = p-value <0.005, *** = p-value <0.0005, and ns = no significance.

In all graphs, error bars represent the standard deviation from the mean.

A key to advancing the clinical development of USP7 inhibitors is identifying malignancies and patient populations that are likely to benefit from USP7 inhibition as a treatment. AML represents an indication with high unmet medical need,[5,38] the vast majority of AMLs are *TP53* WT,[39,40] and prior studies have suggested that AML cells are sensitive to USP7 inhibition.[6,9,14,16] FX1-5303 showed potent anti-proliferative activity in multiple models of AML, including the inhibition of cell lines *in vitro*, tumor growth inhibition of MV4-11 xenografts *in vivo*, and activity against patient samples *ex vivo*. Furthermore, we showed synergy between FX1-5303 and the clinically approved BCL2 inhibitor, venetoclax, in AML cell lines and patient samples and elucidated a mechanism that may explain this synergy. The pharmacokinetic properties of FX1-5303 precluded the evaluation of its activity in combination with venetoclax *in vivo*, since both FX1-5303 and venetoclax are inhibitors of CYP3A4. The identification of USP7 inhibitors with suitable properties for the *in vivo* evaluation of synergistic activity in combination with BCL2 inhibition will be an important area of future research.

Limitations of the study

In the present study, we have introduced a USP7 inhibitor and used this inhibitor as a chemical tool to reveal the molecular and cellular effects of USP7 inhibition and its role in the regulation of p53. Through the use of patient *ex vivo* cells, human AML cell lines, and CDX models, we build evidence for the use of USP7 inhibitors in AML, especially in combination with venetoclax. In each case, the clinical significance of these findings remains unclear since our study was limited to pre-clinical models. Further studies using potent and specific USP7 inhibitors in the clinic are needed to assess the safety of USP7 inhibition and its anti-cancer efficacy in patients with AML.

STAR★METHODS

Detailed methods are provided in the online version of this paper and include the following:

- KEY RESOURCES TABLE
- RESOURCE AVAILABILITY
  - Lead contact
  - Materials availability
  - Data and code availability
- EXPERIMENTAL MODEL AND STUDY PARTICIPANT DETAILS
  - Cell lines
  - Patient-derived cells
  - Animals
  - USP7 protein
- METHOD DETAILS
  - In vitro USP7 activity assay
  - Meso Scale Discovery total p53 assay
  - Cell viability and growth assays
  - DUB selectivity profiling
  - Ex vivo patient sample experiments
  - Compounds
  - 1-((7-(1-(azetidin-3-yl)-6-chloro-1,2,3,4-tetrahydroquinolin-8-yl)thieno[3,2-b]pyridin-2-yl)methyl)pyrrolidine-2,5-dione (FX1-3763)
  - (S)-1-((7-(6-chloro-1-(5-azaspiro[3.4]octan-7-yl)-1,2,3,4-tetrahydroquinolin-8-yl)thieno[3,2-b]pyridin-2-yl)methyl)pyrrolidine-2,5-dione (FX1-5303)
  - FX1-5303/USP7 Co-crystal structure determination
  - Surface plasmon resonance
  - MRC5 and MM.1S Live-Cell Imaging
  - Synergy analysis with Venetoclax
  - Mouse MIC-1 ELISA
  - Western blot analysis
- QUANTIFICATION AND STATISTICAL ANALYSIS

SUPPLEMENTAL INFORMATION

Supplemental information can be found online at https://doi.org/10.1016/j.isci.2024.109693.

ACKNOWLEDGMENTS

We thank Markus Dahlgreen, Heidi Koldsoe, Zef Konst, Mats Svensson, Michael Trzoss, Yan Zhang, Fang-Yu Lin, Jie Xu, Shuping Xu, and Junwei Fu for their contributions to the design and synthesis of inhibitors as well as collaborators at Ubiquigent for DUB selectivity profiling, Wuxi Apptec for the *in vivo* evaluation of inhibitors, and Crelux for SPR measurements and crystal structure determination. We thank James Evans for his support with the Graphical Abstract. We thank Schrodinger and Wuxi Apptec for funding this project.

AUTHOR CONTRIBUTIONS

ASF and KAJ wrote the article in consultation with TL. ASF, KAJ, RP, and TL conceived of, designed, and analyzed *in vitro* and *in vivo* biology experiments. JX, TS, SB, ZX, and XH oversaw compound design and synthesis. XY, SH, HQ, and LF performed *in vitro* biology experiments. SEK and JWT oversaw *ex vivo* patient sample experiments. JB oversaw crystal structure determination. WT, TG, LX, KA, DM, and KKJ conceived of and supervised the project.

DECLARATION OF INTERESTS

KAJ, JX, SB, JB, RP, KA, and KKJ disclose employment with Schrödinger. SH, TS, HQ, LF, TG, and DM disclose employment with Wuxi Apptec. ASF, XH, and WT disclose employment with Schrödinger at the time the research was conducted. TL, ZX, XY, and LX disclose employment with Wuxi Apptec at the time the research was conducted. JX, SB, TS, ZX, and XH report a patent for PCT/US2022/015503 pending.

Received: December 13, 2023
Revised: January 11, 2024
Accepted: April 5, 2024
Published: April 9, 2024

REFERENCES

1. Valles, G.J., Bezsonova, I., Woodgate, R., and Ashton, N.W. (2020). USP7 Is a Master Regulator of Genome Stability. Front. Cell Dev. Biol. *8*, 717. https://doi.org/10.3389/fcell.2020.00717.
2. Wang, Z., Kang, W., You, Y., Pang, J., Ren, H., Suo, Z., Liu, H., and Zheng, Y. (2019). USP7: Novel drug target in cancer therapy. Front. Pharmacol. *10*, 427. https://doi.org/10.3389/fphar.2019.00427.
3. Song, M.S., Salmena, L., Carracedo, A., Egia, A., Lo-Coco, F., Teruya-Feldstein, J., and Pandolfi, P.P. (2008). The deubiquitinylation and localization of PTEN are regulated by a HAUSP-PML network. Nature *455*, 813–817. https://doi.org/10.1038/nature07290.
4. Zhang, L., Wang, H., Tian, L., and Li, H. (2016). Expression of USP7 and MARCH7 is correlated with poor prognosis in epithelial ovarian cancer. Tohoku J. Exp. Med. *239*, 165–175. https://doi.org/10.1620/tjem.239.165.
5. Wang, X., Zhang, Q., Wang, Y., Zhuang, H., and Chen, B. (2018). Clinical significance of ubiquitin specific protease 7 (USP7) in predicting prognosis of hepatocellular carcinoma and its functional mechanisms. Med. Sci. Mon. Int. Med. J. Exp. Clin. Res. *24*, 1742–1750. https://doi.org/10.12659/MSM.909368.
6. Cartel, M., Mouchel, P.-L., Gotanègre, M., David, L., Bertoli, S., Mansat-De Mas, V., Besson, A., Sarry, J.-E., Manenti, S., and Didier, C. (2021). Inhibition of ubiquitin-specific protease 7 sensitizes acute myeloid leukemia to chemotherapy. Leukemia *35*, 417–432. https://doi.org/10.1038/s41375-020-0878-x.
7. Gavory, G., O'Dowd, C.R., Helm, M.D., Flasz, J., Arkoudis, E., Dossang, A., Hughes, C., Cassidy, E., McClelland, K., Odrzywol, E., et al. (2018). Discovery and characterization of highly potent and selective allosteric USP7 inhibitors. Nat. Chem. Biol. *14*, 118–125. https://doi.org/10.1038/nchembio.2528.
8. Turnbull, A.P., Ioannidis, S., Krajewski, W.W., Pinto-Fernandez, A., Heride, C., Martin, A.C.L., Tonkin, L.M., Townsend, E.C., Buker, S.M., Lancia, D.R., et al. (2017). Molecular basis of USP7 inhibition by selective small-molecule inhibitors. Nature *550*, 481–486. https://doi.org/10.1038/nature24451.
9. Lamberto, I., Liu, X., Seo, H.-S., Schauer, N.J., Iacob, R.E., Hu, W., Das, D., Mikhailova, T., Weisberg, E.L., Engen, J.R., et al. (2017). Structure-Guided Development of a Potent and Selective Non-covalent Active-Site Inhibitor of USP7. Cell Chem. Biol. *24*, 1490–1500.e11. https://doi.org/10.1016/j.chembiol.2017.09.003.
10. Li, M., Chen, D., Shiloh, A., Luo, J., Nikolaev, A.Y., Qin, J., and Gu, W. (2002). Deubiquitination of p53 by HAUSP is an important pathway for p53 stabilization. Nature *416*, 648–653. https://doi.org/10.1038/nature737.
11. van Loosdregt, J., Fleskens, V., Fu, J., Brenkman, A.B., Bekker, C.P.J., Pals, C.E.G.M., Meerding, J., Berkers, C.R., Barbi, J., Gröne, A., et al. (2013). Stabilization of the Transcription Factor Foxp3 by the Deubiquitinase USP7 Increases Treg-Cell-Suppressive Capacity. Immunity *39*, 259–271. https://doi.org/10.1016/j.immuni.2013.05.018.
12. Qin, W., Leonhardt, H., and Spada, F. (2011). Usp7 and Uhrf1 control ubiquitination and stability of the maintenance DNA methyltransferase Dnmt1. J. Cell. Biochem. *112*, 439–444. https://doi.org/10.1002/jcb.22998.
13. Tavana, O., Li, D., Dai, C., Lopez, G., Banerjee, D., Kon, N., Chen, C., Califano, A., Yamashiro, D.J., Sun, H., and Gu, W. (2016). HAUSP deubiquitinates and stabilizes N-Myc in neuroblastoma. Nat. Med. *22*, 1180–1186. https://doi.org/10.1038/nm.4180.
14. Ohol, Y.M., Sun, M.T., Cutler, G., Leger, P.R., Hu, D.X., Biannic, B., Rana, P., Cho, C., Jacobson, S., Wong, S.T., et al. (2020). Novel, selective inhibitors of USP7 uncover multiple mechanisms of antitumor activity *in vitro* and *in vivo*. Mol. Cancer Therapeut. *19*, 1970–1980. https://doi.org/10.1158/1535-7163.MCT-20-0184.
15. Schauer, N.J., Liu, X., Magin, R.S., Doherty, L.M., Chan, W.C., Ficarro, S.B., Hu, W., Roberts, R.M., Iacob, R.E., Stolte, B., et al. (2020). Selective USP7 inhibition elicits cancer cell killing through a p53-dependent mechanism. Sci. Rep. *10*, 5324. https://doi.org/10.1038/s41598-020-62076-x.
16. Kategaya, L., di Lello, P., Rougé, L., Pastor, R., Clark, K.R., Drummond, J., Kleinheinz, T., Lin, E., Upton, J.-P., Prakash, S., et al. (2017). USP7 small-molecule inhibitors interfere with ubiquitin binding. Nature *550*, 534–538. https://doi.org/10.1038/nature24006.
17. Khoo, K.H., Verma, C.S., and Lane, D.P. (2014). Drugging the p53 pathway: understanding the route to clinical efficacy. Nat. Rev. Drug Discov. *13*, 217–236. https://doi.org/10.1038/nrd4236.
18. Mullard, A. (2020). p53 programmes plough on. Nat. Rev. Drug Discov. *19*, 497–500. https://doi.org/10.1038/d41573-020-00130-z.
19. Konopleva, M., Martinelli, G., Daver, N., Papayannidis, C., Wei, A., Higgins, B., Ott, M., Mascarenhas, J., and Andreeff, M. (2020). MDM2 inhibition: an important step forward in cancer therapy. Leukemia *34*, 2858–2874. https://doi.org/10.1038/s41375-020-0949-z.
20. Li, X., Yang, S., Zhang, H., Liu, X., Gao, Y., Chen, Y., Liu, L., Wang, D., Liang, Z., Liu, S., et al. (2022). Discovery of Orally Bioavailable N-Benzylpiperidinol Derivatives as Potent and Selective USP7 Inhibitors with In Vivo Antitumor Immunity Activity against Colon Cancer. J. Med. Chem. *65*, 16622–16639. https://doi.org/10.1021/acs.jmedchem.2c01444.
21. Ghanakota, P., Bos, P.H., Konze, K.D., Staker, J., Marques, G., Marshall, K., Leswing, K., Abel, R., and Bhat, S. (2020). Combining Cloud-Based Free-Energy Calculations, Synthetically Aware Enumerations, and Goal-Directed Generative Machine Learning for Rapid Large-Scale Chemical Exploration and Optimization. J. Chem. Inf. Model. *60*, 4311–4325. https://doi.org/10.1021/acs.jcim.0c00120.
22. Abel, R., Wang, L., Harder, E.D., Berne, B.J., and Friesner, R.A. (2017). Advancing Drug Discovery through Enhanced Free Energy Calculations. Acc. Chem. Res. *50*, 1625–1632. https://doi.org/10.1021/acs.accounts.7b00083.
23. Bos, P.H., Houang, E.M., Ranalli, F., Leffler, A.E., Boyles, N.A., Eyrich, V.A., Luria, Y., Katz, D., Tang, H., Abel, R., and Bhat, S. (2022). AutoDesigner, a De Novo Design Algorithm for Rapidly Exploring Large Chemical Space for Lead Optimization: Application to the Design and Synthesis of d-Amino Acid Oxidase Inhibitors. J. Chem. Inf. Model. *62*, 1905–1915. https://doi.org/10.1021/acs.jcim.2c00072.
24. Chauhan, D., Tian, Z., Nicholson, B., Kumar, K.G.S., Zhou, B., Carrasco, R., McDermott, J.L., Leach, C.A., Fulcinniti, M., Kodrasov, M.P., et al. (2012). A Small Molecule Inhibitor of Ubiquitin-Specific Protease-7 Induces Apoptosis in Multiple Myeloma Cells and Overcomes Bortezomib Resistance. Cancer Cell *22*, 345–358. https://doi.org/10.1016/j.ccr.2012.08.007.
25. Yee, K., Papayannidis, C., Vey, N., Dickinson, M.J., Kelly, K.R., Assouline, S., Kasner, M., Seiter, K., Drummond, M.W., Yoon, S.-S., et al. (2021). Murine double minute 2 inhibition alone or with cytarabine in acute myeloid leukemia: Results from an idasanutlin phase 1/1b study. Leuk. Res. *100*, 106489. https://doi.org/10.1016/j.leukres.2020.106489.
26. Daver, N.G., Garcia, J.S., Jonas, B.A., Kelly, K.R., Assouline, S., Brandwein, J.M., Fenaux, P., Olin, R.L., Martinelli, G., Paolini, S., et al. (2019). Updated Results from the Venetoclax (Ven) in Combination with Idasanutlin (Idasa) Arm of a Phase 1b Trial in Elderly Patients (Pts) with Relapsed or Refractory (R/R) AML Ineligible for Cytotoxic Chemotherapy. Blood *134*, 229. https://doi.org/10.1182/blood-2019-123711.

27. Yim, E.-K., and Park, J.-S. (2005). The role of HPV E6 and E7 oncoproteins in HPV-associated cervical carcinogenesis. Cancer Res. Treat. *37*, 319–324. https://doi.org/10.4143/crt.2005.37.6.319.
28. Fan, Y.-H., Cheng, J., Vasudevan, S.A., Dou, J., Zhang, H., Patel, R.H., Ma, I.T., Rojas, Y., Zhao, Y., Yu, Y., et al. (2013). USP7 inhibitor P22077 inhibits neuroblastoma growth via inducing p53-mediated apoptosis. Cell Death Dis. *4*, e867. https://doi.org/10.1038/cddis.2013.400.
29. Lehmann, C., Friess, T., Birzele, F., Kiialainen, A., and Dangl, M. (2016). Superior anti-tumor activity of the MDM2 antagonist idasanutlin and the Bcl-2 inhibitor venetoclax in p53 wild-type acute myeloid leukemia models. J. Hematol. Oncol. *9*, 50. https://doi.org/10.1186/s13045-016-0280-3.
30. Pan, R., Ruvolo, V., Mu, H., Leverson, J.D., Nichols, G., Reed, J.C., Konopleva, M., and Andreeff, M. (2017). Synthetic Lethality of Combined Bcl-2 Inhibition and p53 Activation in AML: Mechanisms and Superior Antileukemic Efficacy. Cancer Cell *32*, 748–760.e6. https://doi.org/10.1016/j.ccell.2017.11.003.
31. Daver, N.G., Pollyea, D.A., Garcia, J.S., Jonas, B.A., Yee, K.W., Fenaux, P., Assouline, S., Vey, N., Olin, R., Roboz, G.J., et al. (2018). Safety, Efficacy, Pharmacokinetic (PK) and Biomarker Analyses of BCL2 Inhibitor Venetoclax (Ven) Plus MDM2 Inhibitor Idasanutlin (idasa) in Patients (pts) with Relapsed or Refractory (R/R) AML: A Phase Ib, Non-Randomized, Open-Label Study. Blood *132*, 767. https://doi.org/10.1182/blood-2018-99-116013.
32. Pan, R., Ruvolo, V.R., Wei, J., Konopleva, M., Reed, J.C., Pellecchia, M., Andreeff, M., and Ruvolo, P.P. (2015). Inhibition of Mcl-1 with the pan-Bcl-2 family inhibitor (-)BI97D6 overcomes ABT-737 resistance in acute myeloid leukemia. Blood *126*, 363–372. https://doi.org/10.1182/blood-2014-10-604975.
33. Yang, H., Filipovic, Z., Brown, D., Breit, S.N., and Vassilev, L.T. (2003). Macrophage inhibitory cytokine-1: a novel biomarker for p53 pathway activation. Mol. Cancer Therapeut. *2*, 1023–1029.
34. Lev Bar-Or, R., Maya, R., Segel, L.A., Alon, U., Levine, A.J., and Oren, M. (2000). Generation of oscillations by the p53-Mdm2 feedback loop: A theoretical and experimental study. Proc. Natl. Acad. Sci. USA *97*, 11250–11255. https://doi.org/10.1073/pnas.210171597.
35. Lahav, G., Rosenfeld, N., Sigal, A., Geva-Zatorsky, N., Levine, A.J., Elowitz, M.B., and Alon, U. (2004). Dynamics of the p53-Mdm2 feedback loop in individual cells. Nat. Genet. *36*, 147–150. https://doi.org/10.1038/ng1293.
36. Batchelor, E., Loewer, A., Mock, C., and Lahav, G. (2011). Stimulus-dependent dynamics of p53 in single cells. Mol. Syst. Biol. *7*, 488. https://doi.org/10.1038/msb.2011.20.
37. Purvis, J.E., Karhohs, K.W., Mock, C., Batchelor, E., Loewer, A., and Lahav, G. (2012). p53 Dynamics Control Cell Fate. Science *336*, 1440–1444. https://doi.org/10.1126/science.1218351.
38. Koenig, K., Mims, A., Levis, M.J., and Horowitz, M.M. (2020). The Changing Landscape of Treatment in Acute Myeloid Leukemia. Am. Soc. Clin. Oncol. Educ. Book *40*, 343–354. https://doi.org/10.1200/EDBK_279129.
39. Barbosa, K., Li, S., Adams, P.D., and Deshpande, A.J. (2019). The role of TP53 in acute myeloid leukemia: Challenges and opportunities. Genes Chromosomes Cancer *58*, 875–888. https://doi.org/10.1002/gcc.22796.
40. Tyner, J.W., Tognon, C.E., Bottomly, D., Wilmot, B., Kurtz, S.E., Savage, S.L., Long, N., Schultz, A.R., Traer, E., Abel, M., et al. (2018). Functional genomic landscape of acute myeloid leukaemia. Nature *562*, 526–531. https://doi.org/10.1038/s41586-018-0623-z.
41. Kurtz, S.E., Eide, C.A., Kaempf, A., Khanna, V., Savage, S.L., Rofelty, A., English, I., Ho, H., Pandya, R., Bolosky, W.J., et al. (2017). Molecularly targeted drug combinations demonstrate selective effectiveness for myeloid- and lymphoid-derived hematologic malignancies. Proc. Natl. Acad. Sci. USA *114*, E7554–E7563. https://doi.org/10.1073/pnas.1703094114.
42. Tyner, J.W., Yang, W.F., Bankhead, A., 3rd, Fan, G., Fletcher, L.B., Bryant, J., Glover, J.M., Chang, B.H., Spurgeon, S.E., Fleming, W.H., et al. (2013). Kinase pathway dependence in primary human leukemias determined by rapid inhibitor screening. Cancer Res. *73*, 285–296. https://doi.org/10.1158/0008-5472.CAN-12-1906.
43. O'Dowd, C.R., Helm, M.D., Rountree, J.S.S., Flasz, J.T., Arkoudis, E., Miel, H., Hewitt, P.R., Jordan, L., Barker, O., Hughes, C., et al. (2018). Identification and Structure-Guided Development of Pyrimidinone Based USP7 Inhibitors. ACS Med. Chem. Lett. *9*, 238–243. https://doi.org/10.1021/acsmedchemlett.7b00512.
44. Winter, G., Waterman, D.G., Parkhurst, J.M., Brewster, A.S., Gildea, R.J., Gerstel, M., Fuentes-Montero, L., Vollmar, M., Michels-Clark, T., Young, I.D., et al. (2018). DIALS: implementation and evaluation of a new integration package. Acta Crystallogr. D Struct. Biol. *74*, 85–97. https://doi.org/10.1107/S2059798317017235.
45. Evans, P.R., and Murshudov, G.N. (2013). How good are my data and what is the resolution? Acta Crystallogr. D Biol. Crystallogr. *69*, 1204–1214. https://doi.org/10.1107/S0907444913000061.
46. McCoy, A.J., Grosse-Kunstleve, R.W., Adams, P.D., Winn, M.D., Storoni, L.C., and Read, R.J. (2007). Phaser crystallographic software. J. Appl. Crystallogr. *40*, 658–674. https://doi.org/10.1107/S0021889807021206.
47. Murshudov, G.N., Skubák, P., Lebedev, A.A., Pannu, N.S., Steiner, R.A., Nicholls, R.A., Winn, M.D., Long, F., and Vagin, A.A. (2011). REFMAC5 for the refinement of macromolecular crystal structures. Acta Crystallogr. D Biol. Crystallogr. *67*, 355–367. https://doi.org/10.1107/S0907444911001314.
48. Bell, J.A., Ho, K.L., and Farid, R. (2012). Significant reduction in errors associated with nonbonded contacts in protein crystal structures: automated all-atom refinement with PrimeX. Acta Crystallogr. D *68*, 935–952. https://doi.org/10.1107/S0907444912017453.
49. Chou, T.-C., and Talalay, P. (1984). Quantitative analysis of dose-effect relationships: the combined effects of multiple drugs or enzyme inhibitors. Adv. Enzym. Regul. *22*, 27–55. https://doi.org/10.1016/0065-2571(84)90007-4.
50. Ianevski, A., Giri, A.K., and Aittokallio, T. (2020). SynergyFinder 2.0: visual analytics of multi-drug combination synergies. Nucleic Acids Res. *48*, W488–W493.

STAR★METHODS

KEY RESOURCES TABLE

REAGENT or RESOURCE	SOURCE	IDENTIFIER
Antibodies		
Anti-HAUSP / USP7 antibody	Abcam	ab108931; RRID: AB_10862844
MDM2	CST	86934S; RRID: AB_2784534
Mcl-1	Santa Cruz	sc-12756; RRID: AB_627915
p53	Santa Cruz	sc-263; RRID: AB_628084
p21	CST	2947S; RRID: AB_823586
Anti-GAPDH	Millipore	MBA374; RRID: AB_2529496
Hsp90	BD Biosciences	610418; RRID: AB_397798
Goat Anti-Rabbit IgG H&L (HRP)	Abcam	ab205718; RRID: AB_2819160
Rabbit Anti-Mouse IgG(H+L)-HRP	SouthernBiotech	6170-05; RRID: AB_2796243
Biological samples		
Human Peripheral Blood Mononueclear Cells	HemaCare	PB009C-3
Patient-derived AML Specimen	Oregon Health & Science University	https://www.ohsu.edu/knight-cancer-institute/leukemia
Chemicals, peptides, and recombinant proteins		
Recombinant human USP7	Boston Biochem	E-519
Ubiquitin-Rhodamine	Boston Biochem	U-555
Idasanutlin	MedChemExpress	HY-15676
Venetoclax	MedChemExpress	HY-15531
Critical commercial assays		
Total p53 Assay	Meso Scale Discovery	K150DBD
CellTiter-Glo 2.0	Promega	G7573
DUBprofiler Panel	Ubiquient	https://www.ubiquigent.com/platform/dubprofiler
CellTiter96, Aqueous One	Promega	G9241
Mouse MIC-1 ELISA Kit	R&D	MDG150
Deposited data		
Crystal Structure of USP7 in complex with FX1-3763	Protein Data Base (PDB)	8D4Z
Experimental models: Cell lines		
MM.1S	ATCC	CRL-2974
RKO	ATCC	CRL-2577
RKO-E6	ATCC	CRL-2578
OCI-AML-3	COBIOER	CPB60817
MV4-11	ATCC	CRL-9591
WI-38	ATCC	CCL-75
HL-60	ATCC	CCL-240
Experimental models: Organisms/strains		
Female CB-17 SCID mice	Shanghai Jihui Laboraotory Care Co, Ltd.	N/A
Software and algorithms		
GraphPad Prism	Dotmatics	https://www.graphpad.com
XLfit	Microsoft Excel	https://www.idbs.com/xlfit/

RESOURCE AVAILABILITY

Lead contact

Further information and requests for resources and reagents should be directed to and will be fulfilled by the lead contact Alan Futran (futran@gmail.com).

Materials availability

There are restrictions to the availability of newly generated compounds and protein constructs due to the lack of an external centralized repository for their distribution. Considerations will be made for the distribution of these materials on reasonable request pending availability and reasonable compensation by requestor for processing and shipping.

Data and code availability

- Crystallographic data for the USP7/FX1-3763 structure have been deposited at wwPDB (PDB code 8D4Z) and are publicly available as of the date of publication. Accession numbers are listed in the key resources table.
- This paper does not report original code.
- Any additional information required to reanalyze the data reported in this paper is available from the lead contact upon request.

EXPERIMENTAL MODEL AND STUDY PARTICIPANT DETAILS

Cell lines

MM.1S (CRL-2974), MV4-11(CRL-9591), HL-60 (CCL-240), RKO (CRL-2577), EKO-E6 (CRL-2578), MRC5 (CCL-171), and WI-38 (CCL-75) cells were acquired from American Type Culture Collection. OCI-AML-3 (CBP60817) cells were acquired from COBIOER and authenticated by STR profiling. Human Peripheral Blood Mononuclear Cells (PB009C-3) were purchased from HemaCare. For maintenance, cells were cultured in a humidified incubator with 5% CO2 at 37°C. MM.1S cells were cultured in RPMI 1640 supplemented with 10% FBS, 1% L-glutamine and 1% penicillin/streptomycin. OCI-AML-3 cells were cultured in RPMI 1640 supplemented with 20% FBS and 1% penicillin/streptomycin. MV4-11 cells were cultured in IMDM supplemented with 10% FBS and 1% penicillin/streptomycin. HL-60 cells were cultured in IMDM supplemented with 20% FBS and 1% penicillin/streptomycin. RKO, RKO-E6, MRC5 and WI-38 cells cultured in EMEM supplemented with 10% FBS and 1% penicillin/streptomycin. Medium and supplements were purchased from Life Technologies except where indicated. Cell lines used in this study were verified to be mycoplasma negative before undertaking any experiments with them.

Patient-derived cells

All patients gave informed consent to participate in this study, which had the approval and guidance of the institutional review boards at Oregon Health & Science University (OHSU). Patient cell characteristics are described in Figure S5B.

Animals

MM.1S and MV4-11 xenograft studies were conducted at WuXi AppTec. All procedures relating to animal handling, care, and treatment in the study were performed according to guidelines approved by the Institutional Care and Use Committee of WuXi AppTec following the guidance of the Association for Assessment and Accreditation of Laboratory Animal Care. Female CB-17 SCID mice were obtained from Shanghai Jihui Laboratory Care Co., Ltd. At the start of the studies, mice were 6-9 weeks old and weighed 18-23 g. Each mouse was inoculated subcutaneously in the right flank with $5x10^6$ MM.1S or $10x10^6$ MV4-11 cells in 0.2 mL PBS mixed with Matrigel (50/50). Mice were randomized and treatment began when tumor volumes reached an average of approximately 105 mm^3 for the MM.1S xenograft study or approximately 120 mm^3 for the MV4-11 xenograft study. Drugs were administered by oral gavage, and tumor and body weight measurements were made twice per week.

USP7 protein

For *in vitro* biochemical assays, recombinant human USP7 was purchased from Boston Biochem where protein was sourced from Spodoptera frugiperda, Sf 21 (baculovirus)-derived human USP7 protein. For crystallography studies, USP7 (207-560) was expressed and purified from *E.coli* BL21 (DE3).

METHOD DETAILS

In vitro USP7 activity assay

Inhibitors were incubated with 167 pM recombinant human USP7 (Boston Biochem, E-519) in 15 uL 0.4% DMSO in reaction buffer (20 mM HEPES pH7.3, 150 mM NaCl, 1 mM TCEP, and 125 ug/mL BSA) in four-fold 10-point dilution series from a top concentration of 2.5 uM in the wells of 384-well plates (Greiner, 781076). Following a 30 min pre-incubation at room temperature, 10 uL ubiquitin-rhodamine (Boston Biochem, U-555) was added to a final concentration of 160 nM and the reaction was allowed to proceed for 90 minutes at room temperature. The reaction was terminated by adding 5 uL 1M acetic acid. Fluorescence intensity was measured on an Envision plate reader (PerkinElmer)

with a 485 nM excitation/520 nM emission optic module. Percent inhibition in each compound-treated well was calculated by comparison to DMSO-treated and no enzyme control wells representing 0% and 100% inhibition, respectively. Converted data were plotted and IC_{50}s were calculated using the XLfit model (205) in Microsoft Excel. Experiments were performed in triplicate with reproducible results.

Meso Scale Discovery total p53 assay

MM.1S cells were plated in 6-well plates ($1x10^6$ cells per well) overnight before being treated with compounds at final concentrations ranging from 20 μM to 0.0003 μM in four-fold, 9-point dilution or DMSO control (0.1% final concentration) for four hours. Cell lysates were prepared with the Meso Scale Discovery assay kit for total p53 in whole cell lysate (K150DBD) according to the manufacturer's instructions. The amount of total p53 detected was plotted and fit using GraphPad Prism for EC50 calculation.

Cell viability and growth assays

MM.1S (3,500 cells/well), RKO (250 cells/well), or RKO-E6 (2,000 cells/well) cells were plated in 40 uL of their complete medium in 384-well black plates (Greiner, 781090). MV4-11 (1,000 cells/well), OCI-AML-3 (1,000 cells/well), and HL-60 (1,000 cells/well) cells were plated in 80 uL of their complete medium in 96-well black plates (Greiner, 655090). Adhesive cells were incubated at 37°C, 5% CO_2 in a humidified atmosphere overnight and suspension cells were plated right before compound treatment. DMSO-solubilized compounds were added using an ECHO 555 acoustic dispenser or pipette. The final DMSO concentration was 0.1% or 0.2% (v/v). After compound treatment, cells were incubated for 120 hours. Experiments were performed in duplicate or triplicate. Cell viability was evaluated by luminescent signal intensity on an Envision plate reader (PerkinElmer) using CellTiter-Glo 2.0 (Promega, G7573). Percent inhibition in each compound-treated well was calculated by comparison to DMSO-treated and no cell control wells representing 0% and 100% inhibition, respectively, and IC_{50} values for each compound were calculated using the XLfit model (205) in Microsoft Excel.

DUB selectivity profiling

Selectivity assays were performed against 44 DUBs available in the DUBprofiler panel at a fixed compound concentration of 10 μM at Ubiquigent.[7]

Ex vivo patient sample experiments

All patients gave informed consent to participate in this study, which had the approval and guidance of the institutional review boards at Oregon Health & Science University (OHSU). *ex vivo* functional drug screens were performed on freshly isolated mononuclear cells from patients with AML and other heme malignancies.[40–42] Briefly, mononuclear cells were isolated by Ficoll gradient centrifugation from freshly obtained bone marrow aspirates or peripheral blood draws and plated within 24 hours. Drug plates were created by distributing a single agent per well in a seven-point concentration series, created from three-fold dilutions of the most concentrated stock resulting in a range of 10 μM to 0.0137 μM. Combinations with venetoclax were performed by adding equimolar FX1-5303 and venetoclax. Cells were seeded into 384-well assay plates at 10,000 cells per well in Roswell Park Memorial Institute (RPMI) 1640 media supplemented with fetal bovine serum (FBS) (10%), l-glutamine, penicillin/streptomycin, and β-mercaptoethanol (10−4 M). After 3 days of culture at 37°C in 5% CO_2, MTS reagent (CellTiter96 AQueous One; Promega) was added, optical density was measured at 490 nm, and raw absorbance values were adjusted to a reference blank value and then used to determine cell viability (normalized to untreated control wells).

Compounds

Idasanutlin (HY-15676) and Venetoclax (HY-15531) were purchased from MedChemExpress. All other chemicals were purchased from commercial suppliers. An inert atmosphere of nitrogen or argon was used for reactions involving air- or moisture-sensitive reagents. Analytical thin layer chromatography (TLC) was performed using 2.5 × 7.5 cm Liang Chen silica gel thin layer plates visualized using combinations of UV visualization, p-anisaldehyde, potassium permanganate, and/or iodine staining. Silica gel column chromatography was performed using Agela RediSep Rf normal phase (40−60 μm) silica gel columns on an Agela CombiFlash Rf or CombiFlash Rf+ purification system (detection at 254 nm). Reversed-phase preparative high-performance liquid chromatography (HPLC) was carried out using a Luna-C18 column (10 μm, 100 × 30 mm, Welch, Shanghai, China) eluting with variant gradients on a Gilson Prep, GX-281 purification system. Analytical reverse-phase HPLC was performed using Xtimate-C18 column (3 μm, 2.1 × 30 mm, Welch, Shanghai, China) eluting with CH_3CN in water with 0.1% TFA on a SHIMADZU LC-2020 purification system (detection at 220 and 254 nm). Proton NMR spectra were recorded on a Bruker AVANCE NEO 400 MHz spectrometer with 5 mm Iprobe and carbon NMR spectra were recorded at 400 MHz. Chemical shifts are expressed in δ ppm referenced to tetramethylsilane (δ = 0 ppm). Abbreviations used in describing peak signal multiplicity are as follows: s = singlet, d = doublet, dd = double doublets, t = triplet, q = quartet, m = multiplet, br = broad peak. Analytical liquid chromatography−mass spectroscopy (LC−MS) was performed using a Xtimate C18 column (2.1 × 30 mm, 3 μm) eluting with a linear gradient from 0 to 30% (solvent B) over 3 minutes and holding at 90% for 0.5 minute at a flow rate of 1.2 mL/min (A = 0.037% TFA in water and B = 0.018 % TFA in acetonitrile) using a SHIMADZU LC-20AB purification system (detection at 220 nm and 254 nm) equipped with a SHIMADZU LCMS-2020in electrospray ionization mode (ESI^+). The purity of all compounds used in bioassays as determined by this method to be >95% pure.

1-((7-(1-(azetidin-3-yl)-6-chloro-1,2,3,4-tetrahydroquinolin-8-yl)thieno[3,2-b]pyridin-2-yl)methyl)pyrrolidine-2,5-dione (FX1-3763)

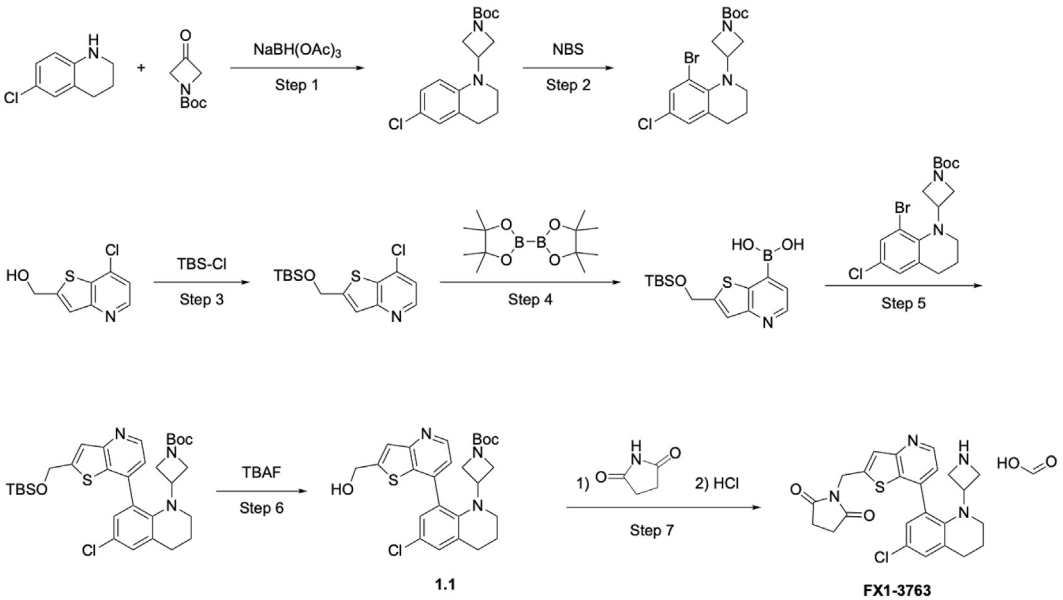

Step 1: *tert*-butyl 3-(6-chloro-3,4-dihydroquinolin-1(2*H*)-yl)azetidine-1-carboxylate

To a solution of 6-chloro-1,2,3,4-tetrahydroquinoline (1.5 g, 8.65 mmol) and *tert*-butyl 3-oxoazetidine-1-carboxylate (2.2 g, 12.97 mmol) in 1,2-dichloroethane (20 mL) and acetic acid (1.0 g) was added sodium triacetoxyborohydride (3.7 g, 17.30 mmol) at 25°C. After stirring at 25°C for 1 h, the mixture was quenched by addition of a saturated aqueous solution of sodium bicarbonate (40 mL) and extracted with ethyl acetate (30 mL x 3). The combined organic layers were washed with brine (60 mL), dried over anhydrous sodium sulfate, filtered and concentrated under reduced pressure to afford the title compound (2.5 g, 90% yield), which was used in the next step without further purification. LCMS R_T = 1.433 min, *m/z* = 323.2 $[M + H]^+$.

Step 2: *tert*-butyl 3-(8-bromo-6-chloro-3,4-dihydroquinolin-1(2*H*)-yl)azetidine-1-carboxylate

To a solution of *tert*-butyl 3-(6-chloro-3,4-dihydro-2*H*-quinolin-1-yl)azetidine-1-carboxylate (2.5 g, 7.74 mmol) in N,N-dimethylformamide (15 mL) was added N-bromosuccinimide (1.4 g, 7.74 mmol) at 25°C. After stirring for 4 min at 25°C, the reaction was quenched by addition of saturated aqueous solution of sodium bicarbonate (40 mL) and extracted with ethyl acetate (30 mL x 3). The combined organic layers were washed with brine (60 mL), dried over anhydrous sodium sulfate, filtered and concentrated under reduced pressure. The residue was purified by column chromatography (silica gel, 100 – 200 mesh, 0 – 10% ethyl acetate in petroleum ether) to afford the title compound (2.5 g, 80% yield). LCMS R_T = 1.521 min, *m/z* = 403.2 $[M + H]^+$.

Step 3: 2-(((*tert*-butyldimethylsilyl)oxy)methyl)-7-chlorothieno[3,2-b]pyridine

To a solution of (7-chlorothieno[3,2-b]pyridin-2-yl)methanol (20.0 g, 100.17 mmol) and imidazole (27.3 g, 400.69 mmol) in dichloromethane (300 mL) was added *tert*-butyldimethylsilyl chloride (37.8 g, 250.43 mmol). After stirring at 25°C for 12 h under nitrogen atmosphere, the reaction mixture was diluted with water (100 mL) and extracted with dichloromethane (200 mL x 2). The combined organic layers were washed with brine (20 mL), dried over anhydrous sodium sulfate, filtered and concentrated under reduced pressure. The residue was purified by column chromatography (silica gel, 100 – 200 mesh, 5 – 30% ethyl acetate in petroleum ether) to afford the title compound (30.0 g, 95% yield). LCMS R_T = 1.615 *m/z* = 314.1 $[M + H]^+$.

Step 4: (2-(((*tert*-butyldimethylsilyl)oxy)methyl)thieno[3,2-b]pyridin-7-yl)boronic acid

To a solution of 2-(((*tert*-butyldimethylsilyl)oxy)methyl)-7-chlorothieno[3,2-b]pyridine (160 mg, 0.51 mmol), bis(pinacolato)diboron (389 mg, 1.53 mmol) and potassium acetate (150 mg, 1.53 mmol) in dioxane (3 mL) was added dichloro[1,1′-bis(diphenylphosphino)ferrocene]palladium(II) (75 mg, 0.10 mmol) under nitrogen atmosphere. After stirring at 140°C for 1 h in a microwave oven, the reaction was filtered and the filtrate was concentrated under reduced pressure to afford the title compound (600 mg, 100% yield), which was used in the next step without further purification. LCMS R_T = 0.873 *m/z* = 324.0 $[M + H]^+$.

Step 5: *tert*-butyl 3-(8-(2-(((*tert*-butyldimethylsilyl)oxy)methyl)thieno[3,2-b]pyridin-7-yl)-6-chloro-3,4-dihydroquinolin-1(2*H*)-yl)azetidine-1-carboxylate

A mixture of *tert*-butyl 3-(8-bromo-6-chloro-3,4-dihydro-2*H*-quinolin-1-yl)azetidine-1-carboxylate (600 mg, 1.49 mmol), [2-[[*tert*-butyl(dimethyl)silyl]oxymethyl]thieno[3,2-b]pyridin-7-yl]boronic acid (482 mg, 1.49 mmol), dichloro[1,1′-bis(diphenylphosphino)ferrocene]palladium(II) (218 mg, 0.3 mmol) and cesium carbonate (973 mg, 2.99 mmol) in water (2 mL) and dioxane (20 mL) was stirred at 110°C for 2 h. The

reaction mixture was diluted with water (30 mL) and extracted with ethyl acetate (30 mL x 2). The combined organic layers were washed with brine (30 mL), dried over anhydrous sodium sulfate, filtered and concentrated under reduced pressure. The residue was purified by column chromatography (silica gel, 100 – 200 mesh, 0 – 20% ethyl acetate in petroleum ether) to afford the title compound (500 mg, 56% yield). LCMS R_T = 1.148 min, *m/z* = 600.2 $[M + H]^+$.

Step 6: *tert*-butyl 3-(6-chloro-8-(2-(hydroxymethyl)thieno[3,2-b]pyridin-7-yl)-3,4-dihydroquinolin-1(2*H*)-yl)azetidine-1-carboxylate

To a solution of *tert*-butyl 3-[8-[2-[[*tert*-butyl(dimethyl)silyl]oxymethyl]thieno[3,2-b]pyridin-7-yl]-6-chloro-3,4-dihydro-2*H*-quinolin-1-yl]azetidine-1-carboxylate (900 mg, 1.50 mmol) in tetrahydrofuran (15 mL) was added tetrabutylammonium fluoride (1.5 mL, 1.0 M in tetrahydrofuran). After stirring for 30 min at 25°C, the reaction mixture was concentrated under reduced pressure. The residue was purified by column chromatography(silica gel, 100 – 200 mesh, 0 – 20% ethyl acetate in petroleum ether) to afford the title compound (350 mg, 48% yield). LCMS R_T = 0.892 min, *m/z* = 486.2 $[M + H]^+$.

Step 7: 1-[[7-[1-(azetidin-3-yl)-6-chloro-3,4-dihydro-2*H*-quinolin-8-yl]thieno[3,2-b]pyridin-2-yl]methyl]pyrrolidine-2,5-dione

To a solution of *tert*-butyl 3-[6-chloro-8-[2-(hydroxymethyl)thieno[3,2-b]pyridin-7-yl]-3,4-dihydro-2*H*-quinolin-1-yl]azetidine-1-carboxylate (150 mg, 0.31 mmol), succinimide (61 mg, 0.62 mmol) and triphenylphosphine (162 mg, 0.62 mmol) in tetrahydrofuran (2 mL) was added diisopropylazodicarboxylate (125 mg, 0.62 mmol) at 0°C. After stirring at 0°C for 10 min, the reaction was concentrated under reduced pressure. The residue was dissolved in dioxane (5 mL) and hydrochloric acid (1.80 mL, 4 M in dioxane) was added. After stirring at 25°C for 30 min, the reaction mixture was concentrated under reduced pressure. The residue was purified by HPLC (15 – 45% acetonitrile in water and 0.225% formic acid) to afford the title compound (44.89 mg, 91% yield). ^{1}H NMR (400MHz, CD_3OD) δ = 8.75 (d, *J* = 5.2 Hz, 1H), 8.53 (s, 1H), 7.60 – 7.38 (m, 2H), 7.21 (s, 2H), 4.97 (s, 2H), 4.07 – 3.98 (m, 1H), 3.50 (br s, 2H), 3.47 – 3.22 (m, 4H) 2.93 (t, *J* = 6.4 Hz, 2H), 2.77 (s, 4H), 1.93 (br. s, 2H). LCMS R_T = 1.550 min, *m/z* = 467.2 $[M + H]^+$.

(S)-1-((7-(6-chloro-1-(5-azaspiro[3.4]octan-7-yl)-1,2,3,4-tetrahydroquinolin-8-yl)thieno[3,2-b]pyridin-2-yl)methyl) pyrrolidine-2,5-dione (FX1-5303)

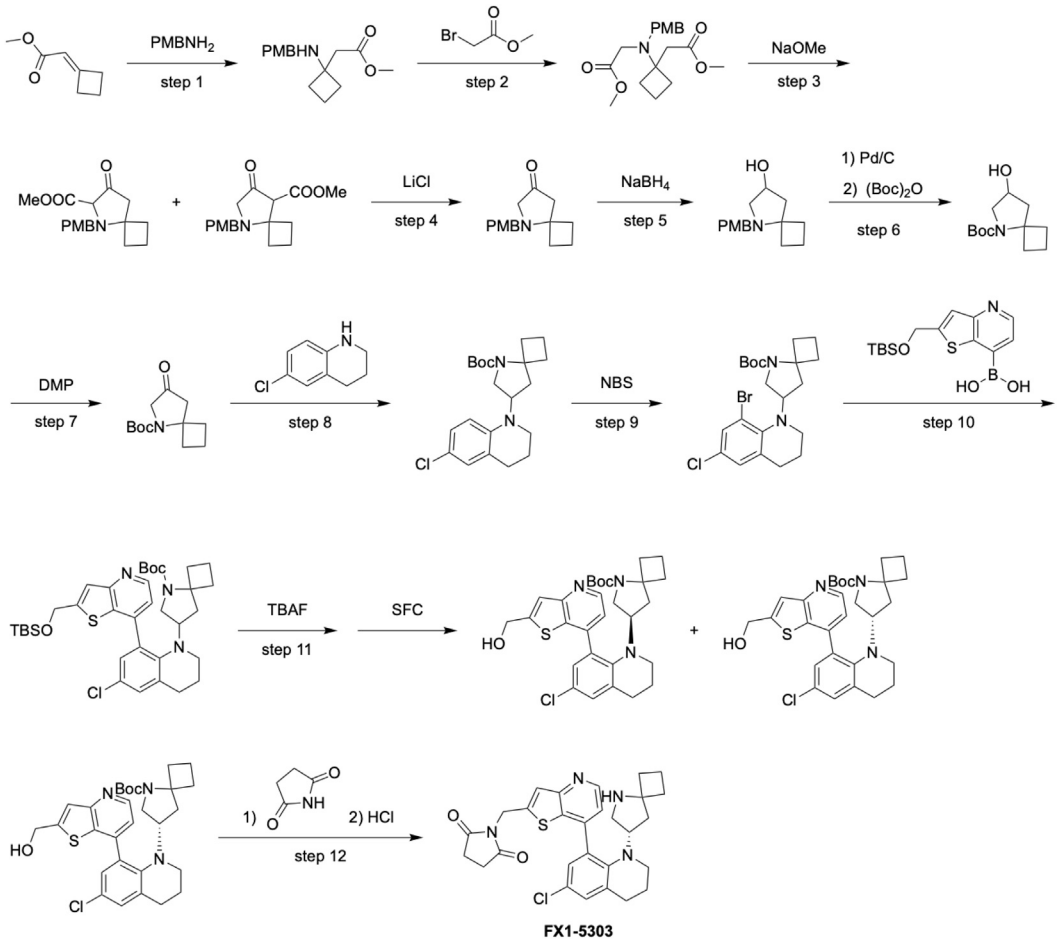

Step 1: methyl 2-(1-((4-methoxybenzyl)amino)cyclobutyl)acetate:

To a solution of methyl 2-cyclobutylideneacetate (15 g, 118.90 mmol) in ethyl alcohol (100 mL) was added (4-methoxyphenyl)methanamine (16.31 g, 118.90 mmol). After stirring at 80°C for 12 h, the reaction mixture was quenched by saturated sodium bicarbonate (40 mL), then the reaction mixture was diluted with water (10 mL), extracted with ethyl acetate (30 mL x 2). The combined organic layers were washed with brine (60 mL), dried over anhydrous sodium sulfate and concentrated under reduced pressure to afford the title compound (30.0g, 100% yield). LCMS R_T = 0.638 min, *m/z* = 264.2 $[M+H]^+$.

Step 2: methyl 2-(1-((2-methoxy-2-oxoethyl)(4-methoxybenzyl)amino)cyclobutyl)acetate:

To a solution of methyl 2-(1-((4-methoxybenzyl)amino)cyclobutyl)acetate (75 g, 284.81 mmol) and sodium bicarbonate (47.85 g, 569.62 mmol) in acetonitrile (400 mL) was added methyl 2-bromoacetate (87.14 g, 569.62 mmol) at 20°C. After stirred at 50°C for 12 h, the reaction mixture was quenched by water (30 mL), then the reaction mixture was diluted with water (10 mL), extracted with ethyl acetate (20 mL x 3). The combined organic layers were washed with brine (60 mL), dried over anhydrous sodium sulfate and concentrated under reduced pressure to give a residue. The residue was purified by column chromatography to afford the title compound (75.0 g, 79% yield). LCMS R_T = 0.779 min, *m/z* = 336.2 $[M+H]^+$.

Step 3: methyl 5-(4-methoxybenzyl)-7-oxo-5-azaspiro[3.4]octane-6-carboxylate and methyl 5-(4-methoxybenzyl)-7-oxo-5-azaspiro[3.4]octane-8-carboxylate

To a solution of methyl 2-(1-((2-methoxy-2-oxoethyl)(4-methoxybenzyl)amino)cyclobutyl)acetate (30 g, 89.45 mmol) in methyl alcohol (200 mL) was added sodium methoxide (24.16 g, 447.24 mmol) at 20°C. After stirring at 60°C for 12 h, the reaction mixture was quenched by water (30 mL), then the reaction mixture was diluted with water (10 mL), extracted with ethyl acetate (20 mL x 3). The combined organic layers were washed with brine (60 mL), dried over anhydrous sodium sulfate and concentrated under reduced pressure to afford the title compound which was used in the next step without further purification (10 g, 37% yield). LCMS R_T = 0.757 min, *m/z* = 304.2 $[M+H]^+$.

Step 4: 5-(4-methoxybenzyl)-5-azaspiro[3.4]octan-7-one

The mixture methyl 5-(4-methoxybenzyl)-7-oxo-5-azaspiro[3.4]octane-6-carboxylate with methyl 5-(4-methoxybenzyl)-7-oxo-5-azaspiro[3.4]octane-8-carboxylate (5 g, 16.48 mmol) was dissolved in dimethyl sulfoxide (5 mL) and water (0.1 mL). After stirring at 130°C for 0.5 h, the reaction mixture was quenched by water (100 mL), extracted with ethyl acetate (50 mL x 3). The combined organic layers were washed with brine (60 mL), dried over anhydrous sodium sulfate and concentrated under reduced pressure. The residue was purified by preparative HPLC to afford the title compound (2.0 g, 49% yield). LCMS R_T = 0.647 min, *m/z* = 246.3 $[M+H]^+$.

Step 5: 5-(4-methoxybenzyl)-5-azaspiro[3.4]octan-7-ol

To a solution of 5-(4-methoxybenzyl)-5-azaspiro[3.4]octan-7-one (2 g, 8.15 mmol) in methyl alcohol (10 mL) was added sodium borohydride (1.01 g, 26.79 mmol). After stirring at 25°C for 16 h, the reaction mixture was concentrated under reduced pressure to give a residue. The residue was purified by preparative HPLC to afford the title compound as a yellow oil (2.0 g, 98% yield).

Step 6: *tert*-butyl 7-hydroxy-5-azaspiro[3.4]octane-5-carboxylate

To a solution of 5-(4-methoxybenzyl)-5-azaspiro[3.4]octan-7-ol (2 g, 8.09 mmol) in methyl alcohol (30 mL) was added 5% palladium carbon (200 mg, 0.81 mmol) at 20°C. After stirring at 20°C for 2 h under hydrogen atmosphere, the reaction mixture was filtered and the filtrate was concentrated under reduced pressure. The residue was dissolved in dichloromethane (10 mL), then triethylamine (1.19 g, 11.79 mmol) and di-*tert*-butyl dicarbonate (2.06 g, 9.44 mmol) was added. After stirring at 20°C for 1 h, the reaction mixture was concentrated under reduced pressure. The residue was purified by column chromatography to afford the title compound as a white solid (1.0 g, 54% yield). LCMS R_T = 0.860 min, *m/z* = 172.2 $[M + H - 56]^+$.

Step 7: *tert*-butyl 7-oxo-5-azaspiro[3.4]octane-5-carboxylate

To a solution of *tert*-butyl 7-hydroxy-5-azaspiro[3.4]octane-5-carboxylate (500 mg, 2.20 mmol) in dichloromethane (10 mL) was added Dess-Martin Periodane (2.80 g, 6.60 mmol) at 20°C. After stirred 20°C for 1 h, the reaction mixture was concentrated under reduced pressure. The residue was purified by column chromatography to afford the title compound as a white solid (450 mg, 91% yield).

Step 8: *tert*-butyl 7-(6-chloro-3,4-dihydroquinolin-1(2*H*)-yl)-5-azaspiro[3.4]octane-5-carboxylate

To a solution of *tert*-butyl 7-oxo-5-azaspiro[3.4]octane-5-carboxylate (400 mg, 1.78 mmol) and 6-chloro-1,2,3,4-tetrahydroquinoline (446 mg, 2.66 mmol) in acetic acid (3 mL) was added sodium borohydride acetate (752 mg, 3.55 mmol) at 20°C. After stirred at 20°C for 1 h, the reaction mixture was concentrated under reduced pressure. The residue was purified by preparative HPLC to afford the title compound as a yellow oil (300 mg, 45% yield). LCMS R_T = 1.223 min, *m/z* = 377.1 $[M+H]^+$.

Step 9: *tert*-butyl 7-(8-bromo-6-chloro-3,4-dihydroquinolin-1(2*H*)-yl)-5-azaspiro[3.4]octane-5-carboxylate

To a solution of *tert*-butyl 7-(6-chloro-3,4-dihydroquinolin-1(2*H*)-yl)-5-azaspiro[3.4]octane-5-carboxylate (100 mg, 0.27 mmol) in dichloromethane (3 mL) was added N-bromosuccinimide (52 mg, 0.29 mmol) at 0°C. After stirred at 0°C for 30 min, the reaction mixture was concentrated under reduced pressure. The residue was purified by pre-TLC to afford the title compound as a yellow oil (100 mg, 83% yield) . LCMS R_T = 1.283 min, *m/z* = 456.9 $[M + 2+H]^+$.

Step 10: *tert*-butyl 7-(8-(2-(((*tert*-butyldimethylsilyl)oxy)methyl)thieno[3,2-b]pyridin-7-yl)-6-chloro-3,4-dihydroquinolin-1(2*H*)-yl)-5-azaspiro[3.4]octane-5-carboxylate

To a solution of *tert*-butyl 7-(8-bromo-6-chloro-3,4-dihydroquinolin-1(2*H*)-yl)-5-azaspiro[3.4]octane-5-carboxylate (100 mg, 0.22 mmol), (2-(((*tert*-butyldimethylsilyl)oxy)methyl)thieno[3,2-b]pyridin-7-yl)boronic acid (106 mg, 0.33 mmol) and cesium carbonate (214 mg, 0.66 mmol) in dioxane (5 mL) and water (0.5 mL) was added dichloro[1,1′-bis(diphenylphosphino)ferrocene]palladium(II) (32 mg, 0.04 mmol) at 20°C. After

stirred at 100°C for 3 h, the reaction mixture was concentrated under reduced pressure. The residue was purified by pre-TLC to afford the title compound as a yellow oil (120 mg, 84% yield). LCMS R_T = 1.221 min, *m/z* = 654.2 $[M+H]^+$.

Step 11: (*S*)-*tert*-butyl 7-(6-chloro-8-(2-(hydroxymethyl)thieno[3,2-b]pyridin-7-yl)-3,4-dihydroquinolin-1(2*H*)-yl)-5-azaspiro[3.4]octane-5-carboxylate

To a solution of *tert*-butyl 7-(8-(2-(((*tert*-butyldimethylsilyl)oxy)methyl)thieno[3,2-b]pyridin-7-yl)-6-chloro-3,4-dihydroquinolin-1(2*H*)-yl)-5-azaspiro[3.4]octane-5-carboxylate (120 mg, 0.18 mmol) in THF (1 mL) was added tetrabutylammonium fluoride in THF (1M, 0.1 mL) at 20°C. After stirred at 20°C for 10 min, the reaction mixture was concentrated under reduced pressure. The residue was purified by preparative TLC (50% ethyl acetate in petroleum ether) to afford the racemic mixture which was subjected to chiral SFC separation (DAICEL CHIRALCEL OJ-H (250 mm*30 mm,10 μm); mobile phase: A: CO_2, B: iso-propanol (0.1% $NH_3 \cdot H_2O$); Gradient: hold 30% of B, flow rate: 80 mL/min) to give first eluting fraction (25 mg, 25% yield, R_t = 2.967 min, LCMS R_T = 0.730 min, *m/z* = 540.2 $[M+H]^+$) and second eluting fraction (25 mg, 25% yield, R_t = 3.541 min, LCMS R_T = 0.730 min, *m/z* = 540.2 $[M+H]^+$).

Step 12: (*S*)-1-((7-(6-chloro-1-(5-azaspiro[3.4]octan-7-yl)-1,2,3,4-tetrahydroquinolin-8-yl)thieno[3,2-b]pyridin-2-yl)methyl)pyrrolidine-2,5-dione

To a solution of (*S*)-*tert*-butyl 7-(6-chloro-8-(2-(hydroxymethyl)thieno[3,2-b]pyridin-7-yl)-3,4-dihydroquinolin-1(2*H*)-yl)-5-azaspiro[3.4]octane-5-carboxylate (25 mg, 0.05 mmol) and succinimide (9 mg, 0.09 mmol) and triphenylphosphine (24 mg, 0.09 mmol) in THF (1 mL) was added diisopropyl azodicarboxylate (18 mg, 0.09 mmol) at 0°C. After stirred at 50°C for 10 min, the reaction mixture was concentrated under reduced pressure. The residue was dissolved in hydrochloric acid in dioxane (4 M, 2 mL). After stirred at 20°C for 10 min, the reaction mixture was concentrated under reduced pressure. The residue was purified by preparative HPLC to afford the title compound as a white solid (4.36 mg, 20% yield). ^{1}H NMR (400MHz, CD_3OD) δ = 8.68 (d, *J* = 4.8 Hz, 1H), 7.52 (s, 1H), 7.44 (d, *J* = 4.8 Hz, 1H), 7.20 – 7.04 (m, 2H), 4.96 (s, 2H), 3.52 – 3.40 (m, 1H), 3.20 (d, *J* = 16.4 Hz, 2H), 2.86 (d, *J* = 4.4 Hz, 2H), 2.76 (s, 5H), 2.04 – 1.72 (m, 5H), 1.64 – 1.16 (m, 6H). LCMS R_T = 1.372 min, *m/z* = 521.3 $[M+H]^+$.

FX1-5303/USP7 Co-crystal structure determination

Protein production, purification, and crystallization were performed by by Crelux GmbH. C-terminal His-tagged USP7 protein was expressed in BL21 (DE3) cells and purified by IMAC and anion exchange chromatography.[7,43] This was followed by size-exclusion chromatography using a column that was equilibrated with 100 mM NaCl, 20 mM Tris-HCl pH 8.0, 4 mM TCEP. Protein at a concentration of 13.26 mg/ml was pre-incubated with 1.6 mM (5.1-fold molar excess) of FX1-3763 (150 mM in DMSO) for 1 h. 0.3 μL of the protein solution was then mixed with 0.02 μl of a seed stocks and 0.58 μL of reservoir solution (0.10 M Bis-Tris-Propane pH 8.50, 0.10 M potassium formate, 26.0% (w/v) PEG 3350) and equilibrated at 20°C over 0.06 mL of reservoir solution. Well diffracting crystals appeared within 4 days and grew to full size over 9 days. Crystals were cryo-protected by addition of 20% glycerol (final concentration) to the crystallization drop before mounting. A complete data set was collected at 100 °K at Petra III (Hamburg, DE, beamline P11) and images were processed using DIALS 1.14.8.[44] The integrated data was reduced and scaled using the AIMLESS procedure.[45] The initial model was obtained by molecular replacement of a model based on PDB entry 5N9R with the program Phaser.[46] Initial structural refinement with REFMAC5[47] was completed using PrimeX.[48]

Surface plasmon resonance

SPR measurements were made by Crelux GmbH using the Biacore 8k (Cytiva) using Stratavidin coated chips (Series S SA chips; Cytiva). Biotinylated avi-tagged USP7 protein was provided by Crelux GmbH. 75 μg/ml protein was injected for 200 sec with a flow rate of 5 μl/min into the active flow cell in SPR running buffer (20 mM HEPES; 150 mM NaCl; 10 mM MgCl2; 0.05 % Tween-20; pH 7.5) at 15°C to reach an immobilization level of about 2000 RU. Small molecules were dissolved and serially diluted 1:1 in 100 % DMSO. After changing the buffer to SPR running buffer with 2 % (v/v) of DMSO, the chip was equilibrated for at least 90 minutes before small molecule samples were applied. The kinetic constants of the small molecules were determined using nine consecutive injections of increasing small molecule concentrations in single cycle kinetic mode at a flow rate of 30 μl/min. The contact time and final dissociation time were 90 sec and 1200 sec respectively. After each cycle, needles were washed with 50% DMSO. A blank run was performed before small molecules were injected. The obtained SPR sensorgrams were analyzed using the Biacore insight evaluation software using double referenced data using the 1:1 binding kinetic binding model.

MRC5 and MM.1S Live-Cell Imaging

Real-time cell growth was monitored using a IncuCyte® S3 Live-Cell Imaging and Analysis instrument (Sartorius) with a 4X objective. MRC5 (4,000 cells/well) and MM.1S (24,000 cells/well) were seeded on 96-well plates (Greiner) overnight before being treated with DMSO, FX1-5303, or Idasanutlin. Images were taken every six hours for 120 hours from the start of the treatment. Analysis was performed using the IncuCyte® ZOOM2020A software and data were presented as phase object confluence.

Synergy analysis with Venetoclax

OCI-AML-3 (1,000 cells/well), MV4-11 (1,000 cells/well), or RKO (500 cells/well) were plated in 80 uL of their complete medium in 96-well black plates (Greiner; 655090). The cells were treated with DMSO or compound pairs in 8 serial dilution doses each, resulting in a 9 × 9 dose combination matrix, for 120 hours. Cell viability was evaluated by the luminescent signal intensity on an Envision plate reader (PerkinElmer) using

CellTiter-Glo 2.0 (Promega, G7573). Percent inhibition in each compound-treated well was calculated by comparison to DMSO-treated and no cell control wells representing 0% and 100% inhibition, respectively, and IC_{50}s were calculated using the XLfit model (205) in Microsoft Excel. To quantify synergy for each combination, combination indices (CI) were calculated.[49] The CI value quantifies synergism, with theoretical additive effect (CI = 1), theoretical antagonism (CI >1), and theoretical synergy (CI <1). We interpreted a CI between 0.8 and 1.2 indicates the two drugs have additive effects when combined, a CI > 1.2 indicates antagonism, and a CI < 0.8 indicates synergy.

Loewe additivity of the combination was visualized using the isobologram method plotted using GraphPad Prism. For this method, the IC_{50}s of each individual drug is plotted as the x or y intercept and the fractional IC_{50}s (IC_{50A}, IC_{50B}) for each combination pair is plotted as a single point. If the fractional IC_{50} values for each combination pair form a straight line connecting the individual drug IC_{50}s, the drug-drug interaction is additive. In contrast, points that fall above that line are antagonistic and points that fall below are synergistic.

Bliss independence analysis was performed and visualized using SynergyFinder 2.0 software[50] to calculate $\boldsymbol{\delta}$ (Excess over Bliss). Theoretical $\boldsymbol{\delta} = 0$ would indicate the actual and expected effects are equivalent and the interaction is additive, whereas $\boldsymbol{\delta} < 0$ indicate antagonism and $\boldsymbol{\delta} > 0$ indicate synergy. We interpreted $\boldsymbol{\delta}$ between -10 and 10 to indicate the interaction is additive, $\boldsymbol{\delta} < -10$ indicates antagonism, and $\boldsymbol{\delta} > 10$ indicates synergy. Because this method does not rely on IC_{50} measurements from dose-response curves, we visualized $\boldsymbol{\delta}$ using a matrix and topology graph. Data presented are representative of at least three independent experiments.

Mouse MIC-1 ELISA

Mouse MIC-1 was quantified using a mouse MIC-1 ELISA kit (R&D#MGD150). Mouse urine samples were centrifuged at 2000 rpm for 5 minutes. From each urine sample, 10 ul was taken and diluted in 490 µL of Calibrator Diluent RD5P (diluted 1:50) on ice. Assay diluent buffer RD1W and standard, control, or sample were added to each well at equal ratio, 50 ul each. The plates were covered and incubated at room temperature for 2 hours on a horizontal orbital microplate shaker set at 500 rpm. After washing, the wells were incubated with 100 uL of mouse/rat GDF-15 conjugate for 2 hours before 100 uL of substrate solution was added and incubated for an additional 30 minutes. The reaction was stopped and the optical density was determined using a microplate reader set to 450 nm and 570 nm. Optical absorbance at 570 nm were subtracted from that at 450 nm. The amount of MIC-1 protein in the urine samples were calculated according to the standard curve.

Western blot analysis

Cell lysates were prepared by treatment with RIPA buffer (Sigma, R0278) for 30 minutes at 4C. Insoluble material was removed from the lysate by centrifugation at 12000-15000 RPM. Tumor lysates were prepared by combining 100mg tumors with 1mL ice-cold RIPA buffer containing 100x protease and phosphatase inhibitor cocktail. Samples were homogenized in a pre-cooled Tissue grinder (JXFSTPRP-CL-48) for 60 seconds at speed 30 HZ/second. After incubating for 30 minutes on ice, insoluble material was removed from the lysate by centrifugation at 12000 RPM. BCA (Pierce#23227) was used for protein quantification and all samples were stored at -80C in western blot loading buffer containing reducing agent.

The lysates were separated using SDS-PAGE (Invitrogen#NP0322BOX) and Western blot analysis using conditions in the table below. Membranes were visualized on an Image Quant LAS 4000 (GE Healthcare Life Sciences) using SuperSignal™ West Dura Extended Duration Substrate (Thermo Scientific; 34076). Protein bands were quantified using ImageJ software. All Western blots were performed and quantified in biological duplicate.

Antibodies	Brand	Catalog number	Diluent	Dilution
Anti-HAUSP / USP7 antibody	Abcam	ab108931	5% BSA	1/500
MDM2	CST	86934S	5% BSA	1/1000
Mcl-1	Santa Cruz	sc-12756	5% BSA	1/500
p53	Santa Cruz	sc-263	5% BSA	1/500
p21	CST	2947S	5% BSA	1/1000
Anti-GAPDH	Millipore	MBA374	5% BSA	1/10000
Hsp90	BD Biosciences	610418	5% BSA	1/2000.
Goat Anti-Rabbit IgG H&L (HRP)	Abcam	ab205718	5% Milk	1/5000.
Rabbit Anti-Mouse IgG(H+L)-HRP	SouthernBiotech	6170-05	5% Milk	1/5000.

QUANTIFICATION AND STATISTICAL ANALYSIS

All statistical analysis was performed using GraphPad Prism. Significance was measured using a multiple unpaired t-test with n=8 animals per group as indicated in the figure legend.